Biophysical Journal Volume 108 February 2015 596–609

Article

Self-Calibrated Line-Scan STED-FCS to Quantify Lipid Dynamics in Model and Cell Membranes

Aleš Benda,[1] Yuanqing Ma,[1] and Katharina Gaus[1,*]
[1]Centre for Vascular Research, Australian Centre for Nanomedicine and ARC Centre of Excellence in Advanced Molecular Imaging, University of New South Wales, Sydney, Australia

ABSTRACT Only a limited number of noninvasive techniques are available to directly measure the dynamic behavior of lipids in model and cell membranes. Here, we explored whether a commercial instrument could be used for fluorescence correlation spectroscopy (FCS) under pulsed stimulated emission depletion (STED). To overcome issues with photobleaching and poor distinction between confocal and STED signals, we implemented resonant line-scan STED with filtered FCS, which has the additional benefit of autocalibrating the dimensions of the point-spread function and obtaining spatially resolved molecular mobility at subdiffraction resolution. With supported lipid bilayers, we achieved a detection spot radius of 40 nm, although at the expense of decreased molecular brightness. We also used this approach to map the dynamics of Atto646N-labeled sphingomyelin and phosphatidylethanolamine in the plasma membrane. Despite the reliability of the method and the demonstration that photobleaching and the photophysical properties of the dye did not influence diffusion measurements, we found great heterogeneities even within one cell. For both lipids, regions of high local density correlated with slow molecular diffusion, indicating trapping of Atto646N-labeled lipids. Future studies with new dyes are needed to reveal the origin of the trapping.

INTRODUCTION

Various concepts of membrane organization, such as the lipid raft hypothesis, have elevated lipids from simple membrane building blocks to regulatory elements (1). It is certainly now appreciated that lipids in biological bilayers can actively contribute to domain formation and membrane compartmentalization (2). However, the tools and techniques for studying lipid domains and the dynamic behavior of lipids in native cell membranes are still in their infancy and consequently relatively little is known about the size, geometry, diversity, and assembly/disassembly rates of lipid domains and complexes, and the ability of these entities to attract and retain other membrane proteins. The limited number of techniques that can be applied equally to model and cell membranes has made it exceedingly difficult to identify which physical mechanisms observed in model membranes are dominant in cell membranes, and how the diversity of cellular lipids preconditions membranes for specific biophysical processes. Often lipid manipulations such as cholesterol depletion are used to infer a role for lipids in distinct biological functions, but in complex membranes, interpretation of the data is often not straightforward (3). Alternatively, the distribution and dynamics of membrane proteins are interpreted as evidence of an underlying lipid organization (4). Thus, it is not surprising that many membrane models still await direct and vigorous testing.

In our opinion, there are two breakthrough technologies that have provided direct insights into the dynamics of single lipids in the plasma membrane of live, unfixed cells. Both employ fluorescent lipid analogs and require a highly sophisticated imaging setup, so experiments involving these approaches have rarely been repeated and expanded to an extended range of lipids. These two technologies are 1) single-molecule tracking at extremely high acquisition speeds to identify lipid hop diffusion (5), in support of the picket-fence membrane model proposed by Kusumi et al. (6); and 2) stimulated emission depletion combined with fluorescence correlation spectroscopy (STED-FCS) (7), in which the reduction of the FCS excitation spot can be used to apply the FCS law (8) and reveal the differential trapping of sphingomyelin (SM) over phosphatidylethanolamine (PE) in cholesterol-dependent domains.

Given that STED instruments are now commercially available, we investigated whether we could implement the STED-FCS technique in such a fashion as to obtain robust and reproducible results regarding lipid diffusion in model and cell membranes. In STED, so-called fluorescence superresolution is achieved by overlaying the excitation beam of a conventional confocal laser scanning microscope with a second laser beam, which reversibly switches off the fluorescence emission in the outer regions of the diffraction-limited focal spot of the excitation laser, thereby reducing the point-spread function (PSF) and vastly improving the spatial resolution (9). In utilizing STED for lipid measurements, we were particularly concerned about the photobleaching effect of the powerful STED laser, since these

Submitted October 10, 2014, and accepted for publication December 3, 2014.

*Correspondence: k.gaus@unsw.edu.au

Editor: Paul Wiseman.

© 2015 by the Biophysical Society
0006-3495/15/02/0596/14 $2.00

http://dx.doi.org/10.1016/j.bpj.2014.12.007

experiments need to be conducted in live, unfixed cells. In addition, since depletion by the STED laser may not result in 100% suppression of fluorescence, the overall emitted light from the sample may be the sum of the fluorescence from the center of the STED doughnut (the superresolution fluorescence that we refer to here as the central spot emission) and the incompletely suppressed fluorescence from the doughnut region of the STED beam (referred to here as the ring emission) (10), decreasing the achievable spatial resolution.

To date, improved lateral resolution by STED has mainly been used in point-acquisition STED-FCS studies (11,12), for STED raster image correlation spectroscopy (STED-RICS) (13), and more recently for pair-correlation analysis (14). By reducing the free diffusion time across the detection spot, the smaller detection spot offered by STED improves the observation window of transient molecular immobilization toward the millisecond timescale, provided the precision and accuracy of the STED-FCS acquisition are sufficiently high. It is well described that point confocal FCS acquisitions require precise calibration of the detection volume (15) and precise z positioning when the lateral diffusion of lipids in membranes is measured (16). Several solutions for the spot size calibration problem have been implemented (16,17). The most practical solution for lateral diffusion measurements is to use scanning FCS (18), particularly line-scan FCS (LS-FCS) (19), which is compatible with commercial instruments. Moreover fast scanning inherently reduces photobleaching of the dye because it reduces the probability of excitation from the triplet state into higher-energy states (20).

Background signals, such as scattered light, detector afterpulsing, and thermal noise, can corrupt the amplitude and shape of autocorrelation functions, leading to errors in the quantification of dye concentrations and time constants of fast dynamics (21). An elegant way to remove the unwanted contributions to the FCS curves is to filter out the background signal based on the time response after pulsed excitation. Enderlein and Gregor (21) showed that photon filtering (weighting) based on the nanosecond time patterns of the fluorescent and background signals can efficiently remove the detector afterpulsing contribution to correlation curves. Štefl et al. (22) demonstrated that photon filtering can be used to extract correlation curves for particular regions of the confocal detection volume, provided the nanosecond time patterns differ at different locations of the confocal volume.

Inspired by solutions developed for traditional confocal FCS, we implemented a fast resonant line scanning and fluorescence filtering approach to overcome the calibration, photobleaching, and background issues encountered with STED-FCS. By calculating spatiotemporal correlations using a newly developed fast correlation algorithm, we can obtain the exact PSF dimension so that the diffusion measurements become autocalibrated and parameters such as fluorophore concentrations, brightness, and diffusion coefficients can be plotted relative to the measured excitation spot area. The fluorescence filtering removes the background signals, which improves the achievable resolution. Additionally, spatially resolved molecular diffusion data are obtained along the scanned line. We applied STED-LS-FCS measurements to DOPE-Atto647N and SM-Atto647N in Cos7 cells and found great heterogeneities even within one cell, where the local concentration of the fluorophores correlated inversely with the diffusion coefficient for both lipids. This meant that fitting of spatiotemporal correlation functions would require one to detect subtle differences between PE and SM dynamics. Hence, we explored other, diffusion-model-free analyses of the same spatiotemporal correlation data, such as image mean-square displacement (iMSD), that might be useful for bridging the data obtained by FCS and single-particle tracking (23).

Theory

A detailed Theory section is provided in the Supporting Material.

MATERIALS AND METHODS

Fluorescent lipid analogs

1,2-Dioleoyl-*sn*-glycero-3-phosphocholine (DOPC) was purchased from Avanti Polar Lipids (Alabaster, AL). DOPE-Atto647N was obtained from ATTO-TEC (Siegen, Germany). Oregon Green 488 DHPE was obtained from Life Technologies. SM-Atto647N was a kind gift from Christian Eggeling, University of Oxford.

Supported lipid bilayers

First, we prepared a 1 mM mixture of DOPC with DOPE-Atto647N, with a ratio of fluorescent dye to lipids of 1:100,000. The organic solvent was evaporated under a stream of nitrogen and the resulting thin lipid film was kept for 2 h under vacuum. The dried lipid film was subsequently hydrated with 10 mM HEPES buffer (150 mM NaCl, pH 7.4) and the solution was extensively vortexed for at least 2 min until multilamellar vesicles were formed. Next, the cloudy solution was extruded by 21 passages through a membrane with a 100 nm pore size (Avanti Polar Lipids), yielding a suspension of large unilamellar vesicles (LUVs). The LUV suspension was diluted in Ca^{2+}-containing buffer (10 mM HEPES, 150 mM NaCl, 1 mM $CaCl_2$, pH 7.4) and incubated on glass surfaces for 30 min. Glass coverslips were used both without and with cleaning (a 20 min exposure to 1 mM NaOH in a sonication bath). Supported lipid bilayers (SLBs) were rinsed to remove excess lipid vesicles and used immediately.

Cell experiments

Cos-7 cells were cultured in high-glucose Dulbecco's modified Eagle's medium (DMEM; Invitrogen) supplemented with 10% fetal calf serum. Cells were plated into a 35 mm glass-bottom culture dish (Proscitech) 24 h before experiments were conducted.

To label cells with fluorescent lipid analogs, 100 nmol of DOPE-Atto647N or SM-Atto647N in chloroform was dried under a nitrogen

stream and redissolved in 20 μl of absolute ethanol by vigorous vortexing. The lipids were diluted to 100 μM with 100 μM defatted bovine serum albumin (BSA; Sigma Aldrich, Australia). The defatted BSA solution was prepared in phenol red-free, 10 mM HEPES-buffered DMEM (Life Technologies, Australia). Cultured cells were washed with ice-cold HEPES-buffered DMEM three times before addition of 50 μM of a lipid-BSA complex solution. Cells were incubated with the lipid-BSA mixture for 30 min and unbound lipids were removed by washing the cells with HEPES-buffered DMEM three times. Finally, the cells were imaged in HEPES-buffered DMEM containing 10% fetal calf serum.

STED-FCS hardware setup

For STED-LS-FCS acquisitions, a commercial Leica SP5 microscope with a near-infrared pulsed STED module and an 8 kHz resonant scanner was used. The excitation sources were pulsed diode lasers (LDH-P-635 and LDH-P-FA-530B) driven by a PDL 800-B (all from PicoQuant, Germany), and the depletion beam was provided by a wavelength-tunable Ti-Sapphire laser (Mai Tai; Spectra Physics). The excitation power varied from 5 to 20 μW and the maximum depletion power was 100 mW for a 750 nm wavelength at the objective back aperture at a frequency of 80 MHz. We mostly used 750 nm rather than 780 nm depletion because it was more than twice as efficient in depleting fluorescence, albeit at the expense of a 10-fold higher anti-Stokes excitation background, which was limited by the available depletion laser power. When a higher signal/noise ratio (SNR) was preferred over the improved resolution, we used depletion at 780 nm. There was no difference in diffusion-related parameters between the data obtained with either depletion wavelength. Synchronization of the excitation and depletion pulses was realized by means of a software-adjustable delay box (Leica). Minor modifications to the excitation path were needed, including insertion of a laser cleanup filter HQ640/10 (Chroma) to suppress the laser diode background, and installation of a motorized microscrew-based control of the excitation intensity (Schaefter and Kirchhoff, Germany) to change the excitation intensity without modifying the excitation pulse time profile. A STED-optimized 100× oil immersion objective with NA 1.4 and 1 Airy unit pinhole size was used. Emitted fluorescence passed an internal 700 nm short-pass filter and an external 680/40 bandpass filter (Chroma), coupled through an optical fiber to a MicroTime200 main optical unit (PicoQuant) containing SPAD detectors (τ-SPAD [PicoQuant, Germany] or PDM [Micro Photon Devices, Italy]). Single photon detection events were saved in a time-tagged time-resolved (TTTR) format with a photon-counting module (PicoHarp300; PicoQuant). In the TTTR data, each photon was encoded by its arrival time after the start of the acquisition, its arrival time after a laser excitation pulse, and its detector number. Additionally, line start markers provided by the Leica trigger box were inserted into the TTTR file for image or LS reconstruction.

After we found the region of interest with *xy* scans, we increased the zoom to a line length of 5.15 μm (80% of amplitude). Next, we initiated continuous bidirectional confocal *xt* scanning with minimized page breaks and optimized the *z* position by minimizing the apparent PSF width, which corresponds to placing the membrane properly into the focused beam waist. After this membrane focusing procedure, we activated the STED laser and started the TTTR data acquisition. Usually, data acquisition took ~1 min for one STED power setting. However, when we tried to reach the minimum spot size using the full laser power at 750 nm depletion (with reduced SNR), the data acquisition was extended up to 5 min.

STED-FCS software

Imaging and setup of the *xt* scans, including STED alignment, were done using standard LAS AF software. For single photon data acquisition in TTTR format, and for online visualization of temporal and spatial correlation functions and other LS-FCS output parameters, an acquisition program with a user interface was written in LabVIEW (NI). The program uses a dll library provided by PicoQuant to operate the PicoHarp300 photon-counting unit and a custom-written dll library for fast spatiotemporal correlations developed in C/C++ (MVS2010; Microsoft). The offline version of this software allows for batch correlations of LS-FCS data in various data formats, application of filtered FCS, correlation data fitting, and iMSD analysis.

Correlation function fitting

The fluorescence cross-correlation function $g(t,\delta)$ between two laterally displaced foci along the x axis by a distance δ is given by (6,24)

$$g(t,\delta) = g_\infty + \varepsilon_1\varepsilon_2 c \int d\boldsymbol{r}_1 \int d\boldsymbol{r}_2 U(\boldsymbol{r}_2)p(\boldsymbol{r}_2 - \boldsymbol{r}_1 - \boldsymbol{x}\delta, t)U(\boldsymbol{r}_1), \quad (1)$$

where g_∞ is the constant offset; ε is the factor that describe the overall excitation power and detection efficiency in the detection volume; c is the concentration of the molecules; $U(r)$ is the molecule detection function (MDF), which gives the position-dependent probability of detecting a fluorescence photon from a molecule at position r (which is equal to the PSF if the molecule responds linearly to excitation intensity); and $p(r_2 - r_1 - x\delta,t)$ denotes the probability density that a molecule will move from position r_2 to position $r_1 + x\delta$ within time t.

Approximating the MDF by a two-dimensional (2D) Gaussian profile and assuming multiple components freely diffusing within the plane, the correlation function takes the form

$$g(t,\delta) = g_\infty + \sum\nolimits_{i=1}^{n} A_i \frac{1}{4D_i t + \omega^2} e^{\left(\frac{-\delta^2}{4D_i t + \omega^2}\right)}, \quad (2)$$

where n is the number of components, A is the amplitude, D is the diffusion coefficient, and ω is the $1/e^2$ radius of the Gaussian beam profile. The full width at half-maximum (FWHM) parameter, which is often used to describe the lateral resolution, is equal to FWHM $= 1.177 \times \omega$. Since the time resolution of the LS is 63 μs and typical triplet relaxation times are on the microsecond timescale, we did not include a triplet term into our model.

If the diffusion is not Brownian, the probability density that a molecule will move from one position to another differs from Green's function for the free diffusion. An example of how this probability density changes and a description of the correlation function when molecules are subject to transient binding at random locations are provided in Dertinger et al. (25).

To fit the intensity-normalized temporal autocorrelation function at different points along the scanned line, we used a simple model for one-component diffusion:

$$G(t) = G_\infty + \frac{1}{PN}\frac{1}{1 + \frac{4Dt}{\omega^2}}, \quad (3)$$

where G_∞ is the correlation function offset, PN is an average particle number in the detection spot, ω is the spot radius, and D is the diffusion coefficient. To estimate the average molecular transit time through the detection spot without any a priori assumption of the diffusion mode, we first fitted the spatial correlation at each lag time to a Gaussian profile to obtain the dependency of the amplitudes on the lag time. The curve was then smoothed with the cubic spline method, and an interpolated value at which the curve decayed to 50% of its zero lag time extrapolated value was read out.

We obtained iMSD plots by fitting a single Gaussian profile to spatial correlations at varying lag times, extrapolating the spot radius to the zero

lag time, and subtracting the obtained initial radius from the radii at varying lag times.

RESULTS AND DISCUSSION

One of the main limitations of quantitative STED measurements is that the PSF dimensions depend on the user-adjusted power of the STED laser and the efficiency of the depletion, which in turn depends on the fluorescent probe as well as on the sample and the focus z position relative to the membrane. To make STED-FCS measurements robust, one must avoid recording each data set with a different PSF and a different degree of suppression of the confocal signal. Hence, recording the STED resolution with a different sample (e.g., with fluorescent beads) is often not practical or reliable, and careful calibration curves need to be recorded (12). These are required because for many measurements, and particularly for the quantification of molecular dynamics and interactions, it is necessary to know the dimensions and localization of the PSF (11).

Here, we used LS-FCS (Fig. 1) to obtain the spatiotemporal correlation function with sufficient sampling, which enabled us to obtain the effective radius of PSF directly from the spatial correlation extrapolated to zero lag time without the need for external calibration. For LS-FCS acquisition of fluorescent lipids (here DOPE-Atto647N) in the plasma membrane, only cells with a sufficiently low labeling density are suitable for correlation analysis (<100 molecules per detection spot is optimal; Fig. 1 *a*). With the plasma membrane adherent to the glass coverslip in focus,

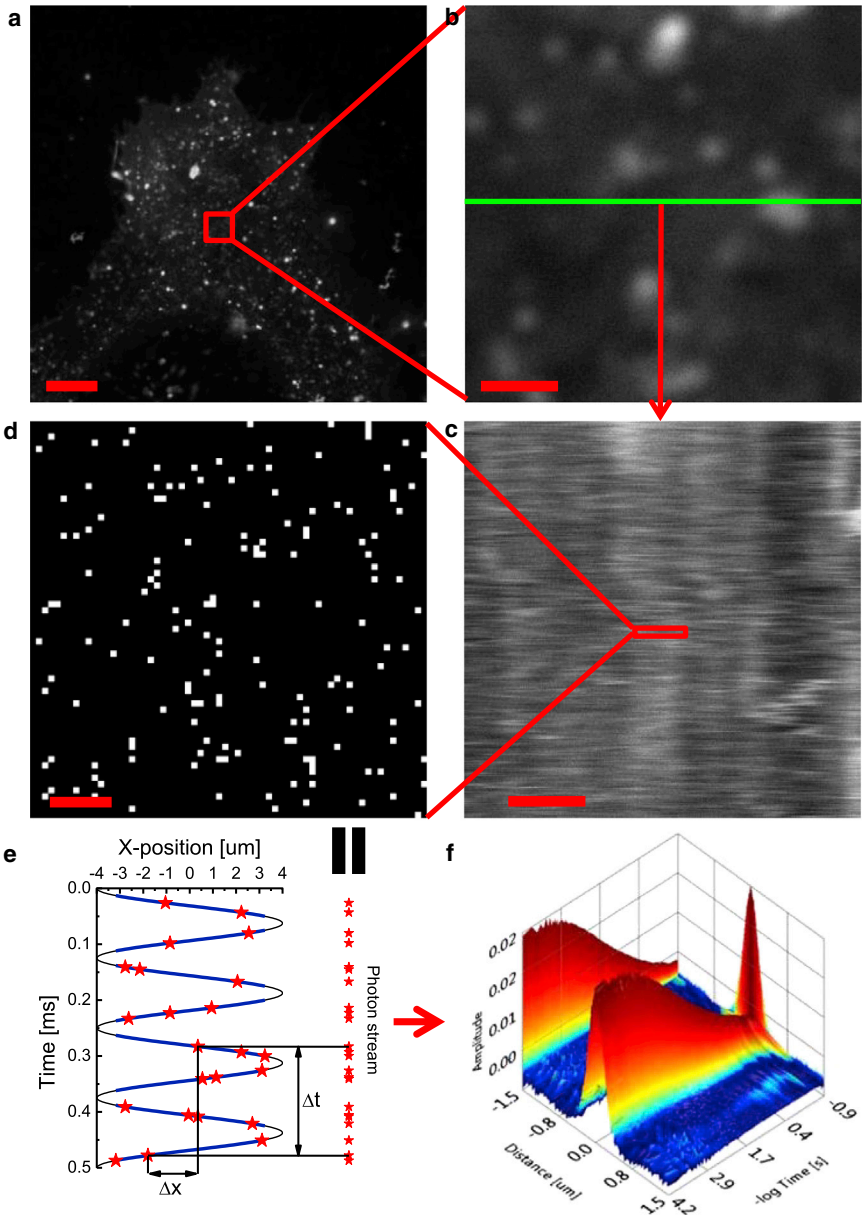

FIGURE 1 Principles of LS-FCS. (*a* and *b*) Intensity images of the plasma membrane adjacent to a glass coverslip in a COS7 cell labeled with DOPE-Atto647N (640 nm excitation at 5 μW). The scale bar represents 10 μm and 1 μm, respectively. (*b*) The highlighted region (*red square* in *a*, 5 μm × 5 μm) is used to select the position of the LS (*green line*). (*c*) Kymograph representing the time evolution of the fluorescence intensity along the scanned line. The scale bar represents 1 μm. A total of 2,170,000 lines were sampled for 137 s at 63 μs per line. At full resolution, each line consists of 2,852 nonequally spaced points. (*d*) A zoomed region of the kymograph reveals the scarcity of detected photons. The scale bar represents 100 nm. (*e*) Individual photons (*stars*) are recorded in a TTTR format and the arrival time of each photon is converted into its exact position along the scanned line (*blue lines*; the *black line* indicates movement of the scanner). The time and position differences, ∂t and ∂x, respectively, from which spatiotemporal correlation curves are calculated are shown for a selected pair of photons. (*f*) Spatiotemporal autocorrelation for DOPE-Atto647N in a COS7 cell from the image shown in (*a*) and (*b*) at confocal (i.e., diffraction-limited) resolution. The projections along the space and time axes are provided to highlight the shape of the autocorrelation function reflecting the time decay and PSF profile, respectively. To see this figure in color, go online.

we selected a region of interest and chose a line within the region (Fig. 1 *b*). We switched the acquisition mode to a continuous bidirectional LS, i.e., an *xt* scan, and visualized the LS as a kymograph (sometimes also called an intensity carpet; Fig. 1 *c*). The kymograph helped us check the quality of the acquired data. In principle, a kymograph acquired by any imaging format allows one to calculate the spatiotemporal correlation function (19).

The correlation function can be calculated by direct multiplication (19) or by a fast Fourier transform (FFT) (26). However, the size of the kymograph at full resolution made it difficult for us to obtain correlation functions from our data by FFT. A 1 min acquisition produces a kymograph of 512 × 960,000 points, which simply takes too long to be processed by FFT on a standard PC. Direct multiplication is also computationally demanding, but it allows for implementation of the multiple-tau algorithm combined with histogramming, similar to the point FCS correlation algorithm described by Felekyan et al. (27). Inspecting the single-line data in more detail revealed that most of the points of the full-resolution kymograph contained zero photons (Fig. 1 *d*). We therefore switched from image-like acquisition to a single-photon acquisition mode using a TTTR format (Fig. 1 *e*). In this mode, every detected photon was assigned a time (t) from the start of the acquisition in multiples of pulsed laser periods, a time (τ) from the excitation laser pulse with picosecond time resolution, and the detector number (d). We could recover the position of the scanner at the time of photon detection using inserted markers, which indicated the start of each scanned line. We then obtained the spatiotemporal correlation function by counting the number of occurrences for a given time (∂t) and position (∂x) difference (Fig. 1 *f*). Hence, this data acquisition format has the additional benefit that the exact position of each photon is known and no binning is required to generate the kymograph. The raw correlation histogram was subsequently corrected for nonlinear motion of the resonant scanner, uneven intensity distribution along the scanned line, and homogeneous photobleaching (Fig. S1). The approach was verified with simulations (Fig. S1), and imaging of nonmobile beads had no temporal or spatial correlations with this approach (Fig. S2). The correlation algorithm is not restricted to TTTR data and can also be used for fast correlation of *xt* scans exported as TIFF images (Fig. S3).

The spatial autocorrelation extrapolated to zero lag time corresponds to a convolution of the PSF with itself (shown as a projection along the time axis in Fig. 1 *f*). Approximating the PSF by a Gaussian, the convolution is also a Gaussian with the radius equal to the square root of two times the PSF radius (as can be seen from Eq. S15 for $t = 0$; see the Theory section in the Supporting Material). Hence, the correlation function directly gives us the effective PSF size without the need for additional calibration experiments. The correlation function at the zero distance is equal to the standard point FCS autocorrelation function (shown as a projection along the distance axis in Fig. 1 *f* and Eq. S15 for $\delta = 0$).

Compared with point FCS acquisition, LS-FCS sacrifices superior time resolution for spatial resolution and averaging. Point FCS allows one to calculate the correlation function at the repetition frequency of the pulsed laser (or the time resolution of the acquisition board for continuous wave (CW) excitation), which was 12.5 ns here for pulsed Ti-Sa STED-FCS. The time resolution of LS-FCS is given by the frequency of the scanner, which was 63 μs for a 7.92 kHz bidirectional scan. The limitation of LS-FCS is that the average residence time of the diffusing molecule in the detection volume must be longer than this time resolution. The diffusion coefficient for lipid translational diffusion in cellular membranes is on the order of $\leq 2\ \mu m^2 s^{-1}$, which results in a correlation time of 5 ms for a diffraction-limited spot of 200 nm radius, and a correlation time of 200 μs for an STED spot of 40 nm radius. This means that LS-FCS at 7.92 kHz scan frequency and spot sizes down to 40 nm can be used to assess lipid diffusion in cells. An additional consideration is the SNR for correlation functions, which is given not only by the brightness of the molecules and the background signal but also by the number of events that caused the fluctuations of the fluorescence signal during the data acquisition. In the case of diffusion measurements, the event that causes fluctuations is the passage of a molecule through the detection spot. Although in general an LS and a point measurement acquire a similar amount of photons, by collecting the signal over larger area, the LS averages more molecular passages. The better averaging of the correlation function allows for shorter acquisition times, especially for slowly diffusing species.

The LS can be considered as a one-dimensional variant of RICS (28,29). In a standard RICS experiment, a series of *xy* images are taken and correlations between neighboring pixels within each image are calculated. The main difference between RICS and LS-FCS is the time and spatial sampling, and hence the resulting spatiotemporal correlation function. In a typical RICS experiment, the time sampling is limited to a couple of points at tens-of-microseconds timescales for neighboring pixel correlations, a couple of points at millisecond time resolution for neighboring lines correlations, and a couple of points at second time resolution for subsequent frames correlations. In contrast to continuous time sampling from 63 μs to seconds in LS-FCS, this sampling is not sufficient to obtain the PSF radius directly from the spatial correlation and must be a known parameter. LS-FCS seems to be a suitable compromise between point FCS and RICS, since it offers a medium spatial averaging with medium temporal resolution and the additional advantage of self-calibration of the PSF radius.

A severe problem in performing accurate STED measurements is background signals that can come from scattered excitation and STED light, dark counts and afterpulsing of the detector, anti-Stokes excitation by STED beam, and

incomplete suppression of the fluorescence in the STED doughnut. The latter is fluorescence (here termed ring emission) that is emitted before the depletion is completed (Fig. 2 *a*), in case of a pulsed depletion or before the depletion is sufficiently high for CW depletion. Such unwanted background signals decrease the resolution (Figs. 2 *e* and S4) and in quantitative FCS measurements lead to an overestimation of the number of the fluorescent molecules.

To minimize the problem with ring emission, we exploited the time-correlated single photon counting (TCSPC) features of the TTTR data acquisition. We generated TCSPC histograms that showed that the photon distribution over time depends on the delay between excitation and depletion pulses (Fig. 2 *b*). The ring emission itself was a fast component in the decay curves (Fig. 2 *c*) and the contribution of the ring emission to the overall signal depended on the delay between excitation and depletion pulses (Fig. 2, *a* and *b*). The more overlapping the pulses were, the more the ring emission was decreased, but it was impossible to remove it completely. The drawback of minimizing the ring emission by higher overlapping of excitation and depletion pulses is that this also lowers the STED efficiency. This is because fluorophores that are excited at the end of the excitation pulse are only exposed to parts of the depletion pulse, so the efficient STED power is lowered and consequently the spatial resolution is decreased. An optimal depletion pulse should arrive only after the excitation pulse is completed, which leads to an increased ring emission, again leading to a decrease in resolution. In practice, one needs to balance these two effects to obtain the highest possible resolution. In our case, the optimal delay was 100 ps when the ring fluorescence was not removed from the correlation function (*solid symbols* in Fig. 2 *e*).

Removal of the ring fluorescence was previously achieved by nanosecond time gating for STED imaging experiments (10), CW STED-FCS acquisition (30), and recently for pulsed STED-FCS experiments (31). The trick behind the time gating is simple: only photons that arrive after the ring fluorescence has decayed are used to calculate the correlation function. However, a more accurate means of distinguishing between photons from the central zero-STED spot and ring emission is photon filtering, an approach that was previously used in fluorescence lifetime correlation spectroscopy (32,33) and more recently in fluorescence spectral correlation spectroscopy (34). In filtered FCS, each photon is weighted according to a filter that splits the signal into its various contributions (here the central spot emission and ring emission, and potentially also the uniform background fluorescence) based on their fluorescence decay patterns. This is possible because the fluorescence decay patterns differ for these two emissions (Fig. 2 *c*). The filters constructed from these decay curves (Fig. 2 *d*) are then used during the calculation of the spatiotemporal correlation functions. We split the original raw correlation function into four filtered correlation functions (Fig. S4) and found that the autocorrelation of the central spot emission with itself had the best spatial resolution. The improvement in spatial resolution due to removal of the ring emission by photon filtering is demonstrated in Fig. 2 *e*. Without filtering, the best resolution in this experiment was 70 nm with a 100 ps delay, whereas with filtering, the resolution was 55 nm for a delay of $\geq$200 ps. The fact that the resolution stayed constant for longer delays after application of the photon filters is in agreement with our assumption that the ring emission is the cause of the decreased spatial resolution. The amount of removed ring emission is the difference between the intensities before and after filtering (Fig. 2 *d*, *blue curves*).

The advantage of filtering over gating is that all photons, even those emitted simultaneously with the background, are used. On the other hand, filtering introduces additional uncertainty and thus decreases the SNR. In general, both gating and filtering achieve similar resolution provided that the afterpulsing of the detector is low, as was the case here. Only in the extreme case of high depletion power (100 mW) and low apparent molecular brightness could we observe a slightly better performance for filtering (improvement from 45 to 40 nm; data not shown), as it also removed the contribution from afterpulsing photons (22). Thus, the main difference between gating and filtering is the SNR of the correlation curves. For dyes with long fluorescent lifetimes (such as Atto647N used in this study) and pulsed depletion, the differences are small. For dyes with a short lifetime, filtering achieves a better SNR than gating. The most significant difference in terms of SNR between gating and filtering can be expected for CW STED depletion with pulsed excitation. Our simulations show that for the same resolution, the relative standard deviation of correlation curves obtained by filtering was almost two times lower than that obtained with gating (Fig. S5).

The primary purpose of STED-FCS is to extend variable-spot FCS (vsFCS) below the diffraction limit (35). In vsFCS, the diffusion coefficients are measured at different length scales and the diffusion mode of the studied molecules is deduced from the dependence of the obtained diffusion coefficients on the measurement spot size (8). Typical modes include free Brownian diffusion, confined diffusion due to domains or meshwork, and temporary binding to immobile structures. For the latter, the sensitivity of the method depends on the ratio of the timescale of the molecular transit time to that of the binding/unbinding event (Fig. S6). If the binding/unbinding event is much faster than the time it takes the molecule to diffuse through the detection spot, it is difficult to distinguish between fast diffusion with temporary trapping and slow diffusion without trapping. Shrinking the detection spot size can thus shorten the average transition time and increase the sensitivity of vsFCS to fast binding/unbinding, as demonstrated by Mueller et al. (7).

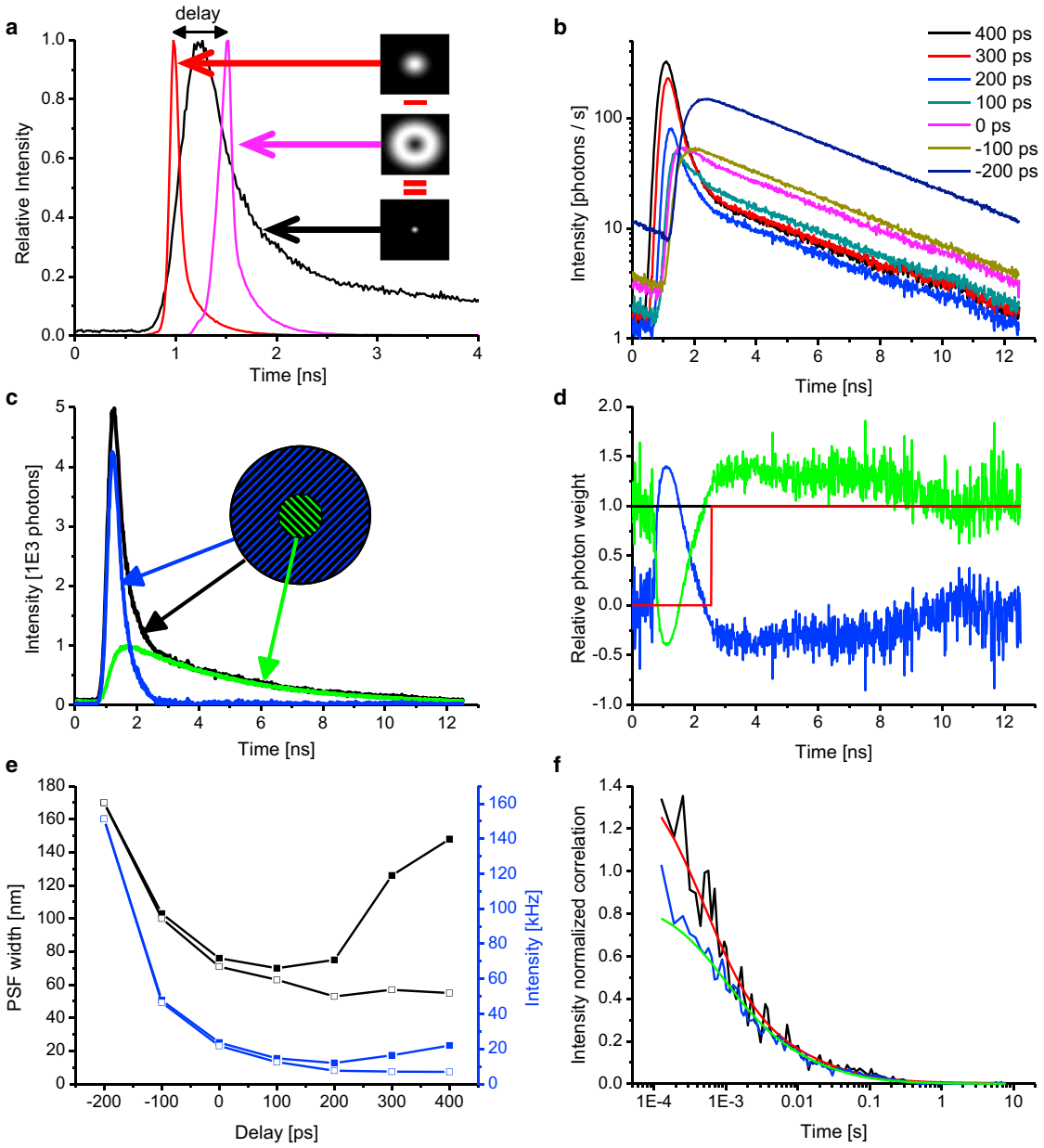

FIGURE 2 STED-FCS with photon weighting improves the spatial resolution and SNR. (*a*) Scheme of the pulsed STED excitation-depletion principle. A focused diffraction-limited 640 nm excitation pulse of 100 ps FWHM (*red line*) is followed by a 750 nm doughnut-shaped STED pulse of 200 ps FWHM (*pink line*). The molecules in the outer ring of the excitation spot are switched off, leading to an improvement in spatial resolution. The overall detected fluoresce decay (*black line*) depends on the delay between the excitation and depletion pulse, and on the excited-state lifetime of the fluorophores. (*b*) TCSPC histograms of DOPE-Atto647N fluorescence in SLBs (DOPC/DOPS at 4:1) for various time delays between the excitation pulse (640 nm, 100 ps FWHM, 10 μW) and the Ti-Sa STED pulse (750 nm, 200 ps FWHM, 50 mW). (*c*) The overall TCSPC histogram (*black line*) from an experiment with an efficient STED depletion can be decomposed into a normally decaying component (*green line*) originating from fluorescence of nondepleted molecules located in the central region and a fast-decaying component (*blue line*) stemming from the ring region before fluorescence depletion. (*d*) Photon-weighting filters calculated from the TCSPC histogram (shown in *c*) for superresolved (*green*) and ring (*blue*) photons that go into the spatiotemporal correlation function calculation. Unlike photon gating (*red line*), photon weighting keeps the overall intensity constant (*black line*). (*e*) Dependence of the spatial resolution (*black line*) and fluorescence intensity (*blue line*) on the delay between excitation and depletion pulses before (*solid squares*) and after (*open squares*) application of the photon-weighting filters shown in (*d*). The best resolution is achieved for delays longer than 200 ps with the ring fluorescence removed by photon weighting. Data are described in (*b*). (*f*) Comparison of temporal correlation decays at zero spatial difference obtained for a 200 ps delay between excitation and depletion pulses without (*blue line*) and with (*black*) photon weighting. Removal of the ring fluorescence increases the amplitude and shortens the correlation time. To see this figure in color, go online.

We tested the STED-vsFCS approach on SLBs labeled with DOPE-Atto647N (Fig. 3). The increase in STED power led to a narrowing of the spatial correlation function, a shortening of the time decays, and an increase in amplitude (Fig. 3, *a–d*). The spatiotemporal correlation functions were fitted to a 2D free-diffusion model with two components (Eq. S15). From the spatial correlations extrapolated to zero lag time, a dependency of the PSF radius on the STED laser power was obtained (Fig. 3 *e*). The shrinking of the detection spot size down to 40 nm was accompanied by a decrease in the apparent molecular brightness. This effect can be explained by nonzero STED intensity in the center of the STED doughnut. Knowing the effective PSF size, we could plot the apparent particle number (Fig. 3 *f*) and diffusion coefficients (Fig. 3 *g*) as a function of the central spot area. The particle number scaled linearly with the spot area unless the latter had a radius of <70 nm. The deviation from linearity at small spot sizes can be explained by the decrease in molecular brightness, since a lower ratio of noncorrelating background to correlating signal increases the apparent particle number. The two diffusion coefficients obtained for the fast and slow fractions differed in their dependence on the spot area (Fig. 3 *g*). The fast diffusion coefficient remained constant, indicating free diffusion. The slow diffusion coefficient decreased with the spot size, indicating temporary binding. It is possible that positively charged DOPE-Atto647N dye becomes transiently arrested on the negatively charged glass surface (25). Hence, this experimental example illustrates both the accuracy and sensitivity of STED-vsFCS measurements obtained using our approach of line scanning and photon weighting.

It is well known that the quality of confocal FCS data acquired on planar membranes crucially depends on the relative axial position of the focal plane and the sample (16). Although LS-FCS mitigates the error of the diffusion coefficient coming from wrong focusing by its internal calibration, we decided to investigate how the STED-FCS data are influenced by changing the axial z position at high STED powers (Fig. S7). The dependencies of the spot radius (*black squares*) and the apparent molecular brightness (*red triangles*) on the z position clearly indicated that there was only a small region in which the measurement was optimal. If the focus is below the membrane, the apparent molecular brightness decreases strongly, which spoils the SNR of the correlation function. If the focus is above the membrane, the molecular brightness also decreases, although not so steeply, and the spatial resolution is compromised as the spot radius increases. The optimal region in these experiments occurred within a 200 nm zone in the axial direction, meaning that a stable stage is required for these measurements (i.e., stage or objective drift should be <200 nm over the acquisition).

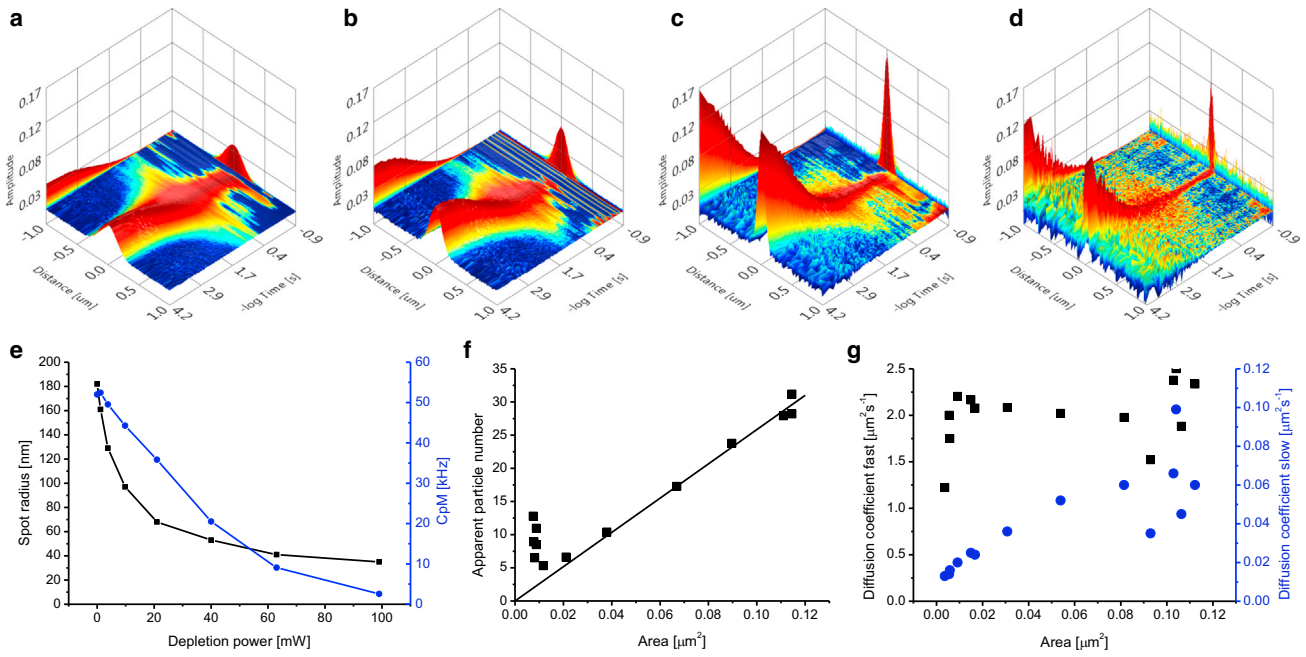

FIGURE 3 STED-vsFCS. (*a–d*) Spatiotemporal correlations for DOPE-Atto647N in SLBs on glass (DOPC/DOPS 4:1, lipid/dye 20,000:1,640 nm excitation at 10 μW) at increasing STED powers: (*a*) 0 mW, (*b*) 5 mW, (*c*) 20 mW, and (*d*) 100 mW. (*e*) Dependence of the effective spot radius (*black squares*) and apparent molecular brightness (*blue circles*) on STED power. The spot radius decreased from 185 nm to 40 nm at the expense of lower molecular brightness. (*f*) The apparent particle number of DOPE-Atto647N is plotted against the spot area. The black line represents the theoretical linear dependence of the particle number on the spot area. (*g*) The spatiotemporal correlation functions at different STED powers were fitted to a two-component model. The obtained fast (*black squares*) and slow (*blue circles*) diffusion coefficients are plotted against the spot area to create a vsFCS plot. To see this figure in color, go online.

An often-discussed issue with STED measurements is the influence of the intensive STED beam on the photophysics and photobleaching of the fluorophores. To demonstrate that the shortening of the correlation function is indeed due only to the diffusion and smaller detection spot size, and not to higher rates of switching into dark states, we adopted a novel (to our knowledge) fit-free concept called area integrated correlation function (AICF) for STED-LS-FCS data. The AICF integrates the values of the spatiotemporal correlation function over the area for varying lag times. In the case of line scanning, the spatiotemporal correlation function is obtained for only one dimension and hence we assume that the correlation function is symmetric within the *xy* plane. For any kind of 2D diffusion, whether Brownian or anomalous, the AICF profile is constant over time as the molecules remain fluorescent within the plane. An AICF profile that decays over time is indicative of other processes, such as out-of-plane diffusion (three-dimensional diffusion), intersystem crossing, and photobleaching. All of these processes cause molecules to disappear from the plane, which leads to the temporal decay of AICF on the timescale of the underlying process. The AICF profile of DOPE-Atto647N in SLBs on glass at various STED powers (Fig. S8, *solid lines*) indicates that the initial STED power-dependent decay of temporal autocorrelation functions (Fig. S8, *dashed lines*) was due to 2D diffusion and not to the photophysical properties of the dye or photobleaching. The changes in the AICF at longer times can be attributed to the increased SNR associated with wider and lower amplitudes in the spatial correlation function.

Having demonstrated the suitability and accuracy of this approach in model membranes, we applied line-scan filtered STED-FCS to cells to further test the method in live biological specimens. We measured and calculated the spatiotemporal correlations with and without STED for a glycophosphatidylinositol (GPI)-anchored protein tag labeled with Atto647N in plasma membrane of HeLa cells (Fig. 4, *a* and *d*), for DOPE-Atto647N in plasma membrane of COS7 cells (Fig. 4, *b* and *e*), and for a membrane-targeted fluorescent protein (Lck10-TagRFP657) in plasma membrane of COS7 cells (Fig. 4, *c* and *f*). For DOPE-Atto647N in plasma membrane of COS7 cells, we reached a resolution of 50 nm, which is similar to that obtained in pure lipid bilayers. For GPI-SNAP-Atto647N, we reached a resolution of 60 nm. With the recently introduced far-red emitting fluorescent protein TagRFP657 (36), we achieved better results with 532 nm excitation than with 640 nm excitation, which allowed us to capture a larger part of the emission spectrum. The resolution for the fluorescent protein improved from 160 nm in confocal mode to 95 nm in STED mode.

Mueller et al. (7) showed that DOPE-Atto647N diffused freely in plasma membrane, whereas SM-Atto647N was subject to temporary binding. We also acquired vsFCS data for DOPE-Atto647N and SM-Atto647N in plasma membrane of COS7 cells. We fitted the spatiotemporal correlation functions by a two-component model and plotted the slow and fast diffusion coefficients versus the effective PSF size (Fig. 5, *a* and *b*). We could not observe any trends for either lipid because of the huge scatter in the data (Fig. 5, *a* and *b*). Therefore, we attempted to discover the source of the scatter. To rule out the possibility that errors were introduced by fitting the data to a two-component model, which may not accurately describe the lipid diffusion modes, we utilized a model-free approach and plotted the average transit time versus the spot area (Fig. S9). However, no trend or clear distinction between DOPE-Atto647N and SM-Atto647N could be seen. There are many possible reasons for this discrepancy between our study and previously published reports (7,11,12), including the use of different cell types (see Conclusions for more details).

Another method for evaluating spatiotemporal correlation data that does not a priori require diffusion models is iMSD (23). This method assesses the time evolution of the MSD of diffusing molecules as the difference between the width of the spatial correlation distribution at the given lag time and the extrapolated distribution width for zero lag time. The widths of the spatial correlation distribution are obtained by fitting single-component Gaussian functions.

The average iMSD curves obtained from the same spatiotemporal correlation data (Fig. 5 *c*) indeed suggest a difference in diffusion between DOPE-Atto647N and SM-Atto647N in cells. The initial slope at short times, proportional to the diffusion coefficient, is similar, but the iMSD curve for SM-Atto647N levels off earlier and at shorter distances than DOPE-Atto647N. Here, we used only one Gaussian function to fit the PSF at any lag time. If there are fast- and slow-diffusing populations, the one-Gaussian fit will return an average PSF width, which depends on the fraction of molecules belonging to either population and also on the lag time. The longer the lag time, the higher is the contribution of the slow fraction to the average PSF width. Taking this interpretation of iMSD plots into account, the earlier leveling off for SM-Atto647N compared with DOPE-Atto647N suggests a higher fraction of slow SM than DOPE molecules. The smaller iMSD values for SM-Atto647N at long lag times could be caused by the much lower mobility of the slow fraction or by the smaller size of the underlying confinement structures.

Similarly to FCS analysis, iMSD analysis could benefit from the smaller PSF size under STED conditions. Smaller detection volumes enhance the relative difference in apparent diffusion coefficients between the bound and free fractions, making the difference detectable. Transient restriction of molecular diffusion leads to irregular widening of the spatial correlation profile, which requires the use of multiple Gaussian functions to describe its profile at times shorter than the time constant of the transient immobilization process. We tested a two-component Gaussian fit of spatial correlations under STED conditions, but the fit parameters were too correlated and did not allow us to quantify

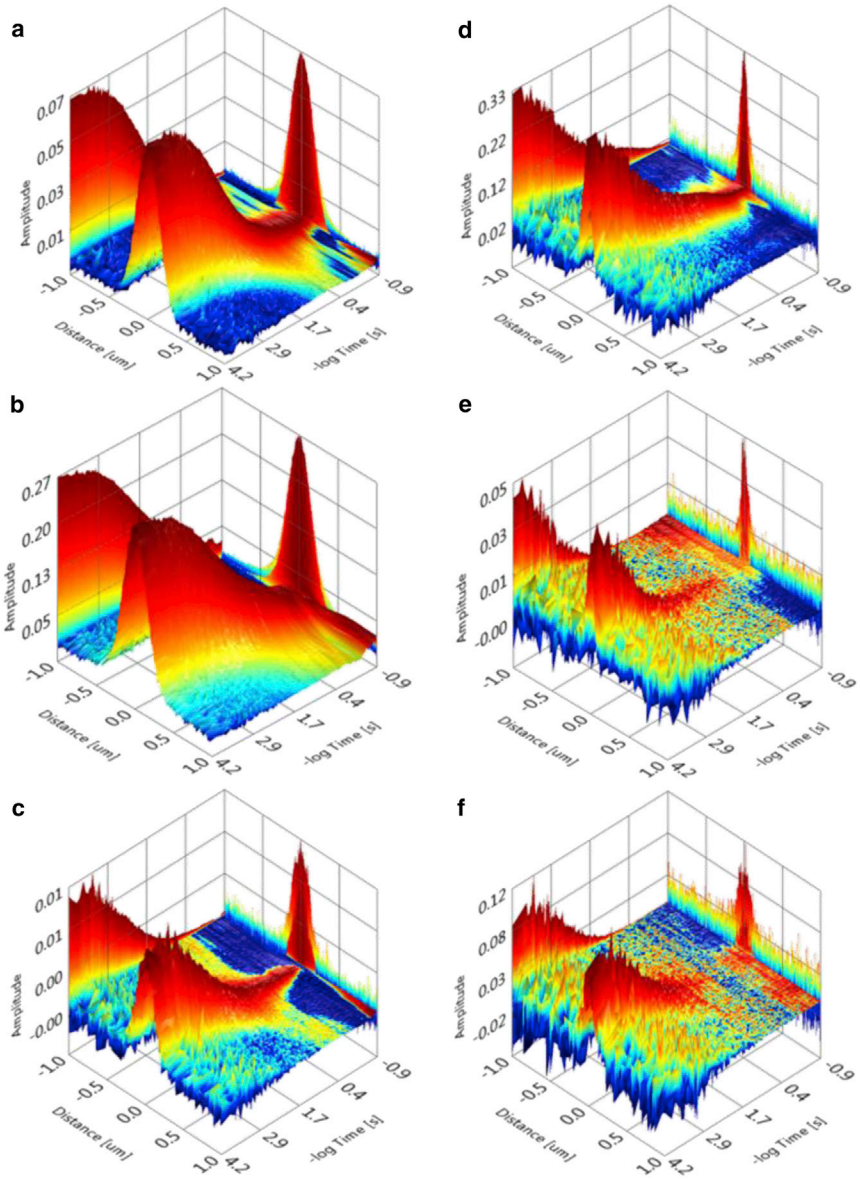

FIGURE 4 Examples of STED-LS-FCS in cells. (*a–c*) Spatiotemporal correlation functions at a confocal resolution of 170–200 nm of (*a*) GPI-SNAP-Atto647 in a HeLa cell (640 nm excitation at 5 μW), (*b*) DOPE-Atto647 in a COS7 cell (640 nm excitation at 5 μW), and (*c*) Lck10-TagRFP647 in a COS7 cell (532 nm excitation at 5 μW). (*d–f*) Spatiotemporal correlation functions with STED for (*d*) GPI-SNAP-Atto647 in a HeLa cell (640 nm excitation at 10 μW, 750 nm depletion at 30 mW) resulting in a resolution of 70 nm; (*e*) DOPE-Atto647 in a COS7 cell (640 nm excitation at 10 μW, 750 nm depletion at 50 mW) at 60 nm resolution; and (*f*) Lck10-TagRFP647 in a COS7 cell (532 nm excitation at 20 μW, 750 nm depletion at 50 mW) with 95 nm resolution. To see this figure in color, go online.

the binding kinetics and reveal any qualitative differences in diffusional properties of SM-Atto647N and DOPE-Atto647N. We propose that a fitting-free analysis of the spatial correlation distributions at different lag times (e.g., based on higher-moments analysis) could potentially provide information on the kinetics of transient immobilization that would complement the results of a STED-FCS analysis. It is possible that the large scatter in the vsFCS plot (Fig. 5, *a* and *b*) of data obtained in cells represents either variations in the membranes themselves or uncertainties in the measurements. To test the robustness of the method in cells, we acquired the full set of vsSTED-FCS data along a single line. As data acquisition for one PSF size (i.e., STED power) typically takes 1–3 min, the single-line vsSTED-FCS experiments took >10 min. Such long acquisition times are impractical because cells can move and fluorophores can bleach during the acquisition. Fig. 5 *d* shows two examples in which we successfully acquired the full vsSTED-FCS series. The constant diffusion coefficient for the fast fraction of DOPE-Atto647N in a COS7 cell (*black squares*) suggests that the method was sufficiently robust, and diffusion of the fast fraction of DOPE-Atto647N molecules was not obstructed. The second example for SM-Atto647N (*red circles*) shows a case in which the apparent diffusion coefficient of the free fraction changed with the spot size, suggesting a temporary binding of the DOPE-Atto647N molecules.

Given the reliability of the measurements themselves, we examined the heterogeneity of diffusion coefficients within a cell in more detail (Fig. 6). The intensity profiles along the scanned line within single acquisitions of DOPE-Atto647N and SM-Atto647N were rarely constant. To find out whether

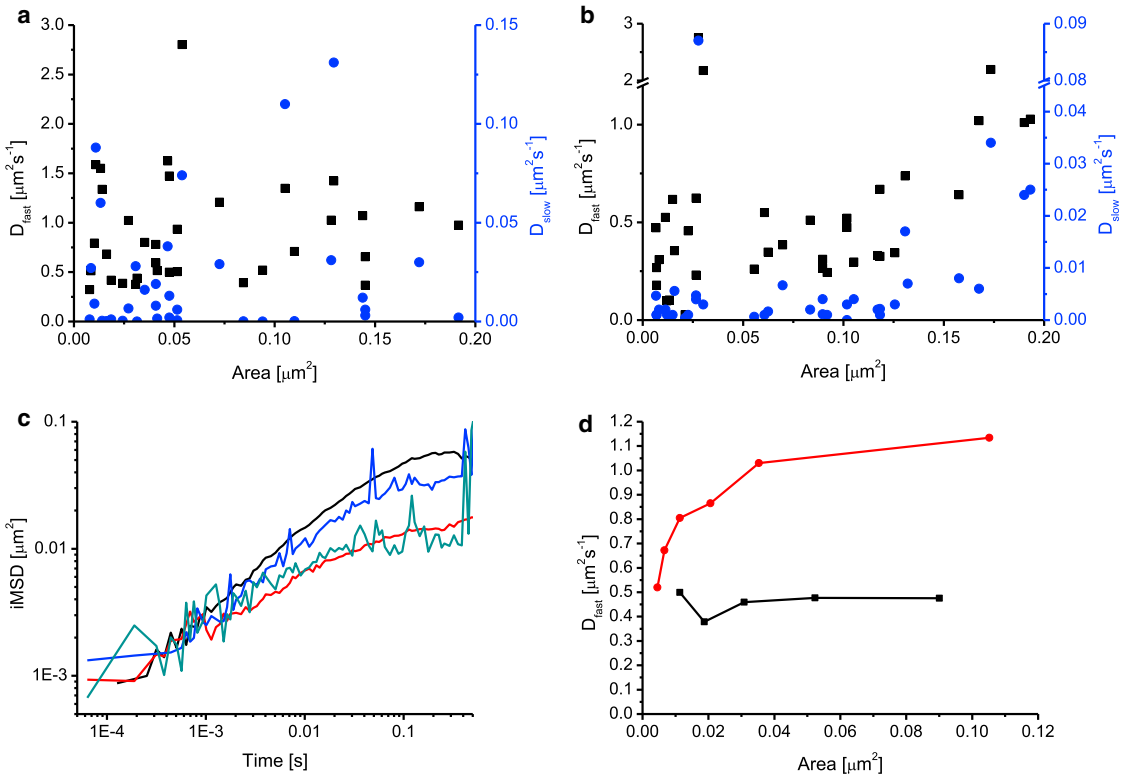

FIGURE 5 STED-vsFCS in cells. (*a* and *b*) The spatiotemporal correlation functions at different STED powers, obtained from COS7 cells labeled with DOPE-Atto647N (*a*) and SM-Atto647N (*b*), were fitted by a two-component model and the obtained fast (*black squares*) and slow (*blue circles*) diffusion coefficients are plotted against the spot area. Each data point represents one STED-LS-FCS acquisition. Data from three different days, with an average of 10 measurements per day, are shown. (*c*) iMSD curves corresponding to data presented in (*a*) and (*b*) are averaged for DOPE-Atto647N and SM-Atto647N, and for confocal (*black and red lines*, respectively) and STED acquisitions (*blue and dark green curves*, respectively). (*d*) Single-line STED-vsFCS experiments for DOPE-Atto647N in COS7 cells (*black line*) and SM-Atto647N in COS7 membrane lawn (*red line*). Line acquisitions at different STED powers were acquired along the same line within one sample. The spatiotemporal correlation functions were fitted to a two-component model and the obtained fast diffusion coefficients were plotted against the spot area. To see this figure in color, go online.

and how heterogeneities in dye density affected the diffusion coefficient, we calculated the temporal correlation functions at different positions along the scanned line, fitted them to a one-component model (Fig. 6, *a* and *b*), and plotted the local diffusion coefficients (*red circles*), dye particle numbers (*blue squares*), and fluorescence intensity (*black line*) against the position in the scanned line for both DOPE-Atto647N and SM-Atto647N (Fig. 6, *c* and *d*). Interestingly, there was a high level of correlation between intensity and particle number, which inversely correlated with the diffusion coefficient. This was observed for both DOPE-Atto647N and SM-Atto647N, and indicates local trapping of Atto647N-labeled molecules, which was independent of the lipid species to which Atto467N was attached. It should be noted that the transiently trapped dye molecules remained mobile. Also, the presence and amount of trapping did not depend on time after the lipid staining, and trapping was present even in the fresh samples taken directly from ice, which suggests that trapping is probably not caused by endocytosis of the Atto647N-labeled lipid molecules. Surprisingly, cells stained with DOPE-Oregon Green 488 did not show this behavior (Fig. S10). As with Atto647N, the intensity profile of DOPE-Oregon Green 488 was not constant and the particle number varied accordingly. However, the diffusion coefficient for DOPE-Oregon Green 488 remained constant within the experimental error, whereas this was not the case for the two Atto647N-labeled lipids (Fig. 6, *c* and *d*). Therefore, we cannot rule out the possibility that the cellular heterogeneities that caused the scatter in the vsFCS plots (Fig. 5, *a* and *b*) were caused by the Atto647N fluorophore itself.

CONCLUSIONS

Here, we utilized a commercial STED microscope with fast resonant line scanning to overcome the key problems of STED-FCS quantification. Our goal was to establish a robust measurement tool for lipid diffusion and, more generally, for biological systems in which transient immobilization of diffusing molecules occurs on timescales shorter than or comparable to the diffusion time of these molecules through the diffraction-limited detection spot. Squeezing down the detection spot significantly shortens the diffusion

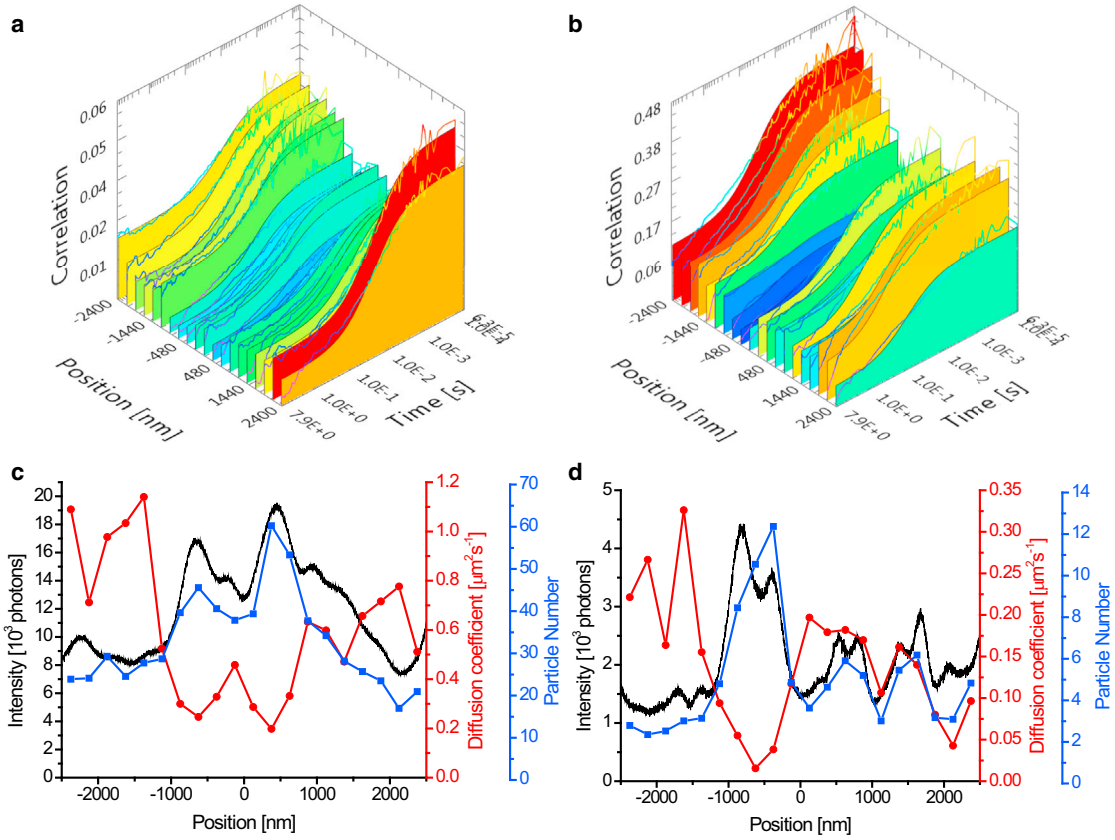

FIGURE 6 Spatially resolved LS-FCS. (*a* and *b*) Examples of temporal autocorrelation functions and their single-component fit at different points along the scanned line for DOPE-Atto647N (*a*) and SM-Atto647N (*b*) in two COS7 cells. Data were acquired at confocal resolution (640 nm excitation at 5 μW). Each of 20 curves is an average of a 250-nm-long line segment. (*c* and *d*) Typical spatial profiles of diffusion coefficients (*red line*) and particle numbers (*blue line*) obtained from single-component fits at different points along the scanned line shown in (*a*) and (*b*), and the corresponding fluorescence intensity (*black line*) for DOPE-Atto647N (*c*) and SM-Atto647N (*d*) in COS7 cells. To see this figure in color, go online.

time but does not change the binding constant of the immobilization. To achieve more reliable STED-FCS measurements and easier quantification, we combined STED excitation with LS-FCS (18,19), which allowed us to determine the PSF size directly from the data and obtain spatially resolved diffusion maps along the scanned line with subdiffraction resolution. Further, we implemented filtered FCS to improve the spatial resolution using TCSPC-based photon filtering, which removes the contributions of nondepleted background fluorescence from the ring regions of the excitation spot. Importantly, this approach also reduces photobleaching and thus enables measurements in bilayers and cells. To our knowledge, we developed a new correlation algorithm to speed up the calculation of high-resolution spatiotemporal correlation functions and tested its robustness against immobile fraction, nonlinear scanning, and homogeneous photobleaching artifacts. We also tested the influence of the axial position on STED-LS-FCS readout parameters and applied AICF to show that the shortening of correlation function with increasing STED power is due to diffusion and not to photobleaching or the photophysics of the dye.

We demonstrated improvements by establishing the spatiotemporal correlation function for lipids and proteins in model and cell membranes. We routinely achieved an effective PSF width of 50 nm in model and cell membranes for Atto647N-labeled lipids. In both model and cell membranes, the spatiotemporal correlation functions required a model with at least two components for fitting. Despite the reliability of the measurements, we found a great heterogeneity in the vsFCS for Atto647N-labeled SM and DOPE both between and within cells. Along a scanned line, the diffusion coefficients of DOPE-Atto647N and SM-Atto647N correlated inversely with local dye concentrations, strongly suggesting that Atto647N-labeled lipids become temporarily trapped. This observation is in agreement with the hydrophobicity and positive charge of Atto647N, which makes the dye prone to sticking to a glass surface and also to unspecific binding to various cellular components (37). The fact that we could detect this heterogeneity, whereas previous point STED-FCS studies did not (11,12), could be due to significant differences between LS-FCS and point FCS with respect to the impact of photobleaching on the data. The LS obtains the same overall

number of photons from a larger number of molecules, resulting in slower local photobleaching rates and superior averaging. With a stationary beam, a bleaching of transiently trapped molecules before they can diffuse away can be expected, and this could prevent one from observing heterogeneity within the sample. Moreover, the slow fraction of diffusing lipids may be less visible in single-point temporal correlation decays and may only become significant when the full spatiotemporal correlation function is analyzed. We should also point out the lipid probes used here are no longer commercially available, so it was not possible to ensure that our probes were identical to those used in the previous studies (7,11,12). Only new STED-compatible fluorophores will reveal whether such trapping is caused by Atto647N interacting with the glass surface or is indeed an intrinsic feature of cell membranes. If it is the latter, a large number of reliable and sensitive measurements will be needed to reveal the complex structure of the cell membranes that cause the lipid trapping behavior. We propose that STED-LS-FCS with the appropriate fluorophores and dependable hardware could provide such data.

SUPPORTING MATERIAL

Supporting Theory, Supporting Materials and Methods, eighteen equations, and ten figures are available at http://www.biophysj.org/biophysj/supplemental/S0006-3495(14)04751-1.

AUTHOR CONTRIBUTIONS

A.B. designed and performed research, contributed analytic tools, analyzed data, and wrote the paper. Y.M. performed research, analyzed data, and contributed to writing of the paper. K.G. designed research and wrote the paper.

ACKNOWLEDGMENTS

We thank the staff of the Biomedical Imaging Facility at the University of New South Wales for support during this study.

A.B. received financial support from the University of New South Wales (Vice-Chancellor's Postdoctoral Fellowship). K.G. received funding from the Australian Research Council (grant number CE140100011 and LP110100390) and the National Health and Medical Research Council of Australia (grant number APP1037320).

SUPPORTING CITATIONS

References (38–43) appear in the Supporting Material.

REFERENCES

1. Simons, K., and M. J. Gerl. 2010. Revitalizing membrane rafts: new tools and insights. *Nat. Rev. Mol. Cell Biol.* 11:688–699.
2. Kraft, M. L. 2013. Plasma membrane organization and function: moving past lipid rafts. *Mol. Biol. Cell.* 24:2765–2768.
3. Goswami, D., K. Gowrishankar, …, S. Mayor. 2008. Nanoclusters of GPI-anchored proteins are formed by cortical actin-driven activity. *Cell.* 135:1085–1097.
4. Fujita, A., J. Cheng, …, T. Fujimoto. 2007. Gangliosides GM1 and GM3 in the living cell membrane form clusters susceptible to cholesterol depletion and chilling. *Mol. Biol. Cell.* 18:2112–2122.
5. Fujiwara, T., K. Ritchie, …, A. Kusumi. 2002. Phospholipids undergo hop diffusion in compartmentalized cell membrane. *J. Cell Biol.* 157:1071–1081.
6. Kusumi, A., C. Nakada, …, T. Fujiwara. 2005. Paradigm shift of the plasma membrane concept from the two-dimensional continuum fluid to the partitioned fluid: high-speed single-molecule tracking of membrane molecules. *Annu. Rev. Biophys. Biomol. Struct.* 34:351–378.
7. Mueller, V., C. Ringemann, …, C. Eggeling. 2011. STED nanoscopy reveals molecular details of cholesterol- and cytoskeleton-modulated lipid interactions in living cells. *Biophys. J.* 101:1651–1660.
8. Wawrezinieck, L., H. Rigneault, …, P. F. Lenne. 2005. Fluorescence correlation spectroscopy diffusion laws to probe the submicron cell membrane organization. *Biophys. J.* 89:4029–4042.
9. Westphal, V., and S. W. Hell. 2005. Nanoscale resolution in the focal plane of an optical microscope. *Phys. Rev. Lett.* 94:143903.
10. Moffitt, J. R., C. Osseforth, and J. Michaelis. 2011. Time-gating improves the spatial resolution of STED microscopy. *Opt. Express.* 19:4242–4254.
11. Eggeling, C., C. Ringemann, …, S. W. Hell. 2009. Direct observation of the nanoscale dynamics of membrane lipids in a living cell. *Nature.* 457:1159–1162.
12. Mueller, V., A. Honigmann, …, C. Eggeling. 2013. FCS in STED microscopy: studying the nanoscale of lipid membrane dynamics. *Methods Enzymol.* 519:1–38.
13. Hedde, P. N., R. M. Dörlich, …, G. U. Nienhaus. 2013. Stimulated emission depletion-based raster image correlation spectroscopy reveals biomolecular dynamics in live cells. *Nat. Commun.* 4:2093.
14. Bianchini, P., F. Cardarelli, …, R. Bizzarri. 2014. Nanoscale protein diffusion by STED-based pair correlation analysis. *PLoS ONE.* 9:e99619.
15. Enderlein, J., I. Gregor, …, J. Fitter. 2004. Art and artefacts of fluorescence correlation spectroscopy. *Curr. Pharm. Biotechnol.* 5:155–161.
16. Benda, A., M. Beneš, …, M. Hof. 2003. How to determine diffusion coefficients in planar phospholipid systems by confocal fluorescence correlation spectroscopy. *Langmuir.* 19:4120–4126.
17. Dertinger, T., V. Pacheco, …, J. Enderlein. 2007. Two-focus fluorescence correlation spectroscopy: a new tool for accurate and absolute diffusion measurements. *ChemPhysChem.* 8:433–443.
18. Ruan, Q., M. A. Cheng, …, W. W. Mantulin. 2004. Spatial-temporal studies of membrane dynamics: scanning fluorescence correlation spectroscopy (SFCS). *Biophys. J.* 87:1260–1267.
19. Ries, J., S. Chiantia, and P. Schwille. 2009. Accurate determination of membrane dynamics with line-scan FCS. *Biophys. J.* 96:1999–2008.
20. Donnert, G., C. Eggeling, and S. W. Hell. 2009. Triplet-relaxation microscopy with bunched pulsed excitation. *Photochem. Photobiol. Sci.* 8:481–485.
21. Enderlein, J., and I. Gregor. 2005. Using fluorescence lifetime for discriminating detector afterpulsing in fluorescence-correlation spectroscopy. *Rev. Sci. Instrum.* 76:033102.
22. Štefl, M., A. Benda, …, M. Hof. 2014. The fast polarization modulation based dual-focus fluorescence correlation spectroscopy. *Opt. Express.* 22:885–899.
23. Di Rienzo, C., E. Gratton, …, F. Cardarelli. 2013. Fast spatiotemporal correlation spectroscopy to determine protein lateral diffusion laws in live cell membranes. *Proc. Natl. Acad. Sci. USA.* 110:12307–12312.
24. Gregor, I., D. Patra, and J. Enderlein. 2005. Optical saturation in fluorescence correlation spectroscopy under continuous-wave and pulsed excitation. *ChemPhysChem.* 6:164–170.
25. Dertinger, T., I. von der Hocht, …, J. Enderlein. 2006. Surface sticking and lateral diffusion of lipids in supported bilayers. *Langmuir.* 22:9339–9344.

26. Hebert, B., S. Costantino, and P. W. Wiseman. 2005. Spatiotemporal image correlation spectroscopy (STICS) theory, verification, and application to protein velocity mapping in living CHO cells. *Biophys. J.* 88:3601–3614.
27. Felekyan, S., R. Kühnemuth, …, C. A. M. Seidel. 2005. Full correlation from picoseconds to seconds by time-resolved and time-correlated single photon detection. *Rev. Sci. Instrum.* 76:083104.
28. Brown, C. M., R. B. Dalal, …, E. Gratton. 2008. Raster image correlation spectroscopy (RICS) for measuring fast protein dynamics and concentrations with a commercial laser scanning confocal microscope. *J. Microsc.* 229:78–91.
29. Digman, M. A., C. M. Brown, …, E. Gratton. 2005. Spatio-temporal fluorescence fluctuation analysis of paxillin-EGFP in cellular adhesions using scanning FCS, ICS and PCH. *Biophys. J.* 88:372a.
30. Vicidomini, G., G. Moneron, …, S. W. Hell. 2011. Sharper low-power STED nanoscopy by time gating. *Nat. Methods.* 8:571–573.
31. Göttfert, F., C. A. Wurm, …, S. W. Hell. 2013. Coaligned dual-channel STED nanoscopy and molecular diffusion analysis at 20 nm resolution. *Biophys. J.* 105:L01–L03.
32. Böhmer, M., M. Wahl, …, J. Enderlein. 2002. Time-resolved fluorescence correlation spectroscopy. *Chem. Phys. Lett.* 353:439–445.
33. Kapusta, P., R. Macháň, …, M. Hof. 2012. Fluorescence lifetime correlation spectroscopy (FLCS): concepts, applications and outlook. *Int. J. Mol. Sci.* 13:12890–12910.
34. Benda, A., P. Kapusta, …, K. Gaus. 2014. Fluorescence spectral correlation spectroscopy (FSCS) for probes with highly overlapping emission spectra. *Opt. Express.* 22:2973–2988.
35. Ringemann, C., B. Harke, …, C. Eggeling. 2009. Exploring single-molecule dynamics with fluorescence nanoscopy. *New J. Phys.* 11:103054.
36. Morozova, K. S., K. D. Piatkevich, …, V. V. Verkhusha. 2010. Far-red fluorescent protein excitable with red lasers for flow cytometry and superresolution STED nanoscopy. *Biophys. J.* 99:L13–L15.
37. Kolmakov, K., V. N. Belov, …, S. W. Hell. 2010. Red-emitting rhodamine dyes for fluorescence microscopy and nanoscopy. *Chemistry.* 16:158–166.
38. Vicidomini, G., A. Schönle, …, S. W. Hell. 2013. STED nanoscopy with time-gated detection: theoretical and experimental aspects. *PLoS ONE.* 8:e54421.
39. Wohland, T., R. Rigler, and H. Vogel. 2001. The standard deviation in fluorescence correlation spectroscopy. *Biophys. J.* 80:2987–2999.
40. Dertinger, T., I. Gregor, …, J. Enderlein. 2006. Measuring precise diffusion coefficients with two-focus fluorescence correlation spectroscopy. *Proc. SPIE.* 6092. http://dx.doi.org/10.1117/12.651053.
41. Benda, A., V. Fagul'ová, …, M. Hof. 2006. Fluorescence lifetime correlation spectroscopy combined with lifetime tuning: new perspectives in supported phospholipid bilayer research. *Langmuir.* 22:9580–9585.
42. Gregor, I., and J. Enderlein. 2007. Time-resolved methods in biophysics. 3. Fluorescence lifetime correlation spectroscopy. *Photochem. Photobiol. Sci.* 6:13–18.
43. Felekyan, S., S. Kalinin, …, C. A. M. Seidel. 2009. Filtered FCS and species cross correlation function. *Proc. SPIE.* 7183. http://dx.doi.org/10.1117/12.814876.

Self-calibrated, line-scan STED-FCS to quantify lipid dynamics in model and cell membranes

Aleš Benda, Yuanqing Ma and Katharina Gaus

Centre for Vascular Research, Australian Centre for Nanomedicine and ARC Centre of Excellence in Advanced Molecular Imaging, University of New South Wales, Sydney NSW
[#] **Correspondence to**: k.gaus@unsw.edu.au

THEORY

Resonant line-scan spatio-temporal correlation function calculation

Line-scan FCS is based on the spatio-temporal correlation of fluorescence intensities obtained by fast scanning of a detection volume along a fixed line within a sample (1). The time evolution of spatially dependent fluorescence intensity can be visualized by an *xt* image, also called kymograph or intensity carpet (Fig 1c,d). By correlating the kymograph data in both dimensions, a spatio-temporal correlation *G(kΔx,lΔt)* is obtained:

$$G(k\Delta x, l\Delta t) = \left(\sum_{i=0}^{n_x-1} \sum_{j=0}^{n_t-1} I(i,j) I(i+k, j+l) \right) \frac{n_x}{n_x - |k|} \frac{n_t}{n_t - |l|} \qquad (1)$$

where *Δx* is a pixel size, *Δt* is the time difference between two consecutive lines (line time), *k* and *l* are integer indexes of distance and time, *I(i,j)* is the intensity value of pixel *i* and *j* in the kymograph, n_x is the total number of pixels and n_t is the total number of lines.

The correlation function can be calculated by direct multiplication (1) or by fast Fourier transform (2). These straightforward approaches can be directly applied to intensity *xt* images obtained by standard acquisition software and are not limited to single photon counting detection. The pixel size should be much smaller than the radius of the detection spot and the maximal spatial distance for which the correlation is calculated should cover distances that the molecules can diffuse across within the acquisition time. The spacing of time correlation points must range from single line time to overall acquisition time. Typically this is best achieved by using a multiple-tau correlation scheme. However, the direct calculation of spatio-temporal correlation covering the required spatial and time resolution is extremely time consuming. Hence we introduced a new faster algorithm based on single photon data format.

The fluorescence intensity is detected as single photon events and stored in a time-tagged time resolved data format with inbuilt markers for synchronization with the scanner (TTTR, PicoQuant, Germany). In the case of a resonant scanner, the position *a* of the focus is a sine function of time *t*:

$$a = A\sin(2\pi f t + \varphi) \qquad (2)$$

Where *A* is the amplitude, *f* is the resonant frequency of the scanner and ϕ is the phase shift. The amplitude *A* depends on the zoom and the objective used. The typical settings of the zoom at 30-times in conjunction with a 1.4NA 100x oil immersion objective give an amplitude of 3217 nm. The resonant frequency of the used scanner was 7920 Hz. The basic unit of lag-time is equal to the line period, which is 63 µs for a bidirectional scan at 7920 Hz.

In accordance with the multiple-tau correlation scheme, the temporal sampling consists of several levels of linear ranges, each range having double the sampling of the previous level. The spatial sampling is given by the frequency of the pulsed excitation laser or the photon detection unit for cw excitation. The finite time sampling means that the photon detection positions are finite as well, giving a definite number of realizations for each distance difference.

The spatio-temporal correlation function is calculated from raw TTTR data in the following steps:

1. The start times of each forward and backward line are obtained from the synchronization markers. This involves interpolation of markers' time to compensate for the 1 MHz markers under-sampling and a phase shift correction. The phase shift as determined from calibration is typically -0.8434. Phase shift calibration is based on maximizing temporal correlation function at zero distance between forward and backward lines for lag times up to 16 lines.
2. Knowing the line start times, each photon is assigned a line (time) number and a precise position along the scanned line.
3. A histogram $H(\delta,\tau)$ of time τ and position δ differences is obtained by comparing line numbers and positions of all photons.

$$H(\delta,\tau) = \sum_{i=0}^{n}\sum_{j=0}^{n,j\neq i}\begin{cases} w_i w_j \text{ if } \left(\delta-\frac{\Delta}{2}\right) < (a_i - a_j) < \left(\delta+\frac{\Delta}{2}\right) \text{ and } \left(\tau-\frac{T}{2}\right) < (t_i - t_j) < \left(\tau+\frac{T}{2}\right) \\ 0 \quad \text{elsewhere} \end{cases} \quad (3)$$

where n is the total number of photons, w_i is the photon weight (intensity), a_i is the position and t_i is the time of i-th detection event, Δ is the spatial correlation sampling and T is the temporal sampling for the given correlation level.

The histogram is calculated for linear spacing of distances and semi-logarithmic spacing in time (multiple-tau algorithm). The algorithm accepts real values of photon intensity, which makes it suitable for photon weighting required for filtered FCS.

4. The correlation function is obtained by correcting the values in a histogram with the relative number of possible occurrences of the given distance-time pair compared to zero distance zero time difference pair. The spatial correction $C_S(\delta)$ is derived from a possible number of realizations of the given distance δ and corrects for both nonlinear scanner motion and average intensity line profile, and is given by: $C_s(\delta) =$

$$\sum_{i=0}^{m}\sum_{j=0}^{m,j\neq i}\begin{cases} I_i I_j \text{ if } \left(\delta-\frac{\Delta}{2}\right) < (a_i - a_j) < \left(\delta+\frac{\Delta}{2}\right) \\ 0 \quad \text{elsewhere} \end{cases} \quad (4)$$

where m is the number of sampling points covering the selected part of the scanned line, I_i is the overall intensity in the given sampling point, a_i is the position of the sampling point and Δ is the spatial correlation sampling.

The time correction $C_T(\tau)$ accounts for varying temporal sampling of correlation function, for finite length of the measurement and is given by:

$$C_T(\tau) = (floor\left(\frac{t}{T}\right) - \tau/T)/T^2 \quad (5)$$

where t is the total measurement time in number of lines and T is the temporal sampling for the given correlation level in number of lines.

The corrected spatio-temporal correlation function $G(\delta,\tau)$ is then given by:

$$G(\delta,\tau) = H(\delta,\tau)\frac{C_S(0)}{C_S(\delta)}\frac{C_T(0)}{C_T(\tau)} \quad (6)$$

5. The optional correction for homogenous photobleaching is based on the fact that the decrease in the average number of dye molecules in the detection spot as measurement progresses only changes the non-correlated offset at different lag times for raw correlation data without intensity normalization. The offset for each lag time is estimated directly from the correlation function, assuming that at long distances there is no correlation at full time scale. The photobleaching corrected spatio-temporal correlation function $G_{PC}(\delta,\tau)$ is then given by:
$$G_{PC}(\delta,\tau) = G(\delta,\tau) + G(\delta_{max},0) - G(\delta_{max},\tau) \quad (7)$$
where δ_{max} is the maximal distance for which the correlation function was calculated.
6. The final step is an optional intensity normalization, in which first a constant offset is subtracted from the correlation function and the result is then divided by the constant offset. As a result the amplitude of correlation function is inversely proportional to the number of dye molecules in the detection spot. The intensity normalized spatio-temporal correlation function $G_{IN}(\delta,\tau)$ is then given by
$$G_{IN}(\delta,\tau) = (G(\delta,\tau) - G(\delta_{max},0))/G(\delta_{max},0) \quad (8)$$

The presented correlation function calculation scheme is not restricted to TTTR or other single photon data acquisition formats, but can also be used for *xt* image based data formats. First the pixel shift is determined by maximizing temporal correlation function at zero distance between odd and even (forward and backward) lines for lag times up to 16. In a second step *xt* images are converted to single photon format. The weight of the photon is an intensity of the pixel. Zero pixel intensity means that no photon event is generated. The number of the pixel is converted to a position and the line number into its time.

Filtered FCS

Filtered FCS (fFCS) is a more general term for mathematically identical fluorescence lifetime correlation spectroscopy (FLCS) (3, 4), originally invented under the name time-resolved fluorescence correlation spectroscopy (5). The difference is that in the case of FLCS the species are resolved based on differences in their excited state lifetime behavior, whereas in the more general case of filtered FCS the species are resolved based on their different patterns in multichannel detection. The different patterns also include different excited state lifetimes, but in addition to that they can also include spectral differences (6), anisotropy differences (7) and spatial excitation modulation differences (8).

Briefly at every time t, the fluorescence intensity $I_j(t)$ in each detection channel j is a linear combination of area normalized detection patterns p_j^k :

$$I_j(t) = \sum_{k=1}^{n} w^k(t)\, p_j^k \quad (9)$$

where k stands for a particular emitter with a specific detection pattern, n is the number of different emitters with different detection patterns and $w^k(t)$ is the contribution of the k^{th} fluorescent species to the total fluorescence signal at time t.

Equation. (1) is an over-determined set of linear equations, provided the number of detection channels is higher than the number of different emitters. Assuming that the photon detection obeys a Poissonian distribution and applying singular value decomposition, the solution of the Eq. (1) can be written as follows:

$$w^k(t) = \sum_{j=1}^{N} f_j^k I_j(t) \tag{10}$$

where N is the number of detection channels and f_j^k is a discrete filter function, which is constructed from the area normalized detection patterns of the different fluorescence species and the total intensities of the compound signal in detection channels. Explicitly, f_j^k is given by:

$$f_j^k = \left(\left[\hat{M}^T \cdot diag \left\langle I_j(t) \right\rangle_t^{-1} \cdot \hat{M} \right]^{-1} \cdot \hat{M}^T \cdot diag \left\langle I_j(t) \right\rangle_t^{-1} \right)_{kj} \tag{11}$$

where the matrix elements are:

$$\hat{M}_{jk} = p_j^k \tag{12}$$

Finally, the intensity normalized correlation function of the k^{th} species with l^{th} species (for auto-correlation $k = l$, for cross-correlation $k \neq l$) is calculated as:

$$G^{kl}(\tau) = \frac{\left\langle w^k(t) w^l(t+\tau) \right\rangle_t}{\left\langle w^k(t) \right\rangle_t \left\langle w^l(t) \right\rangle_t} = \frac{\sum_{i=1}^{N} \sum_{j=1}^{N} f_i^k f_j^l \left\langle I_i(t) I_j(t+\tau) \right\rangle_t}{\sum_{i=1}^{N} \sum_{j=1}^{N} f_i^k f_j^l \left\langle I_i(t) \right\rangle_t \left\langle I_j(t) \right\rangle_t} \tag{13}$$

In the case of pulsed excitation and pulsed STED detection (Figure 2) the first pattern p_1 corresponding to super-resolved emission is obtained from the experimental excited state decay without any STED applied. The decay pattern p_2 for the ring emission is then obtained by subtracting a scaled super-resolution pattern $a^* p_1$ from the overall average experimental decay $<I(t)>$. The scaling factor a is obtained by fitting the tail of the overall average experimental decay $<I(t)>$ with the super-resolved pattern p_1. This procedure is based on the fact that after the STED pulse is over, the measured fluorescence decay returns to its intrinsic kinetics. Here, tail-fitting was usually performed for decay between 3 ns – 12.5 ns.
For the case of pulsed excitation and cw STED depletion the overall average experimental decay $<I(t)>$ was fitted by a sum of three exponentials. The value of the longest lifetime influences the resulting spatial resolution and can be fixed during the excited state decay fitting. Reconstructed decay for every lifetime component corresponds to one pattern p_i. For simulations the instrument response function (IRF) was a delta function.
The correlation function with the best spatial resolution is obtained as an autocorrelation function of the super-resolved pattern for the pulsed depletion or of the pattern with the longest lifetime for cw depletion.

ADDITIONAL MATERIALS AND METHODS

Line-scan gated STED with pulsed excitation and cw depletion

Line-scan FCS data analysis is not limited to pulsed excitation and pulsed depletion, and to TTTR data acquisition format. A proof-of-principle experiment measuring diffusion coefficients of DOPE-Atto488 in SLBs on glass (DOPC:DOPS 4:1, lipid to dye ratio 1:50 000) at and below diffraction limited resolution was performed using a commercial setup for gated-STED (SP5, Leica, Germany) in the test facility at Leica Microsystems in Mannheim. The commercial gated-STED microscope uses pulsed excitation together with cw depletion and gated detection to improve the spatial resolution (9).

The acquisition settings were: excitation by 30% intensity of 494 nm spectral band of white-light laser at 80 MHz, depletion by 100 mW cw laser at 592 nm (STED only), HyD detector operated at 750V with a 1-6.5 ns gate, detection bandpass 500-585 nm, notch filter for 488 and 592 nm, xt scan frequency 8000 Hz (resonant scanner), bidirectional scan, 512 pixels per line, 29.7 nm per pixel (15.2 µm total length, zoom 10.2), 100x 1.4 NA oil STED objective. The measurement time was 60 s and data were exported as 117 pc of xt scan (512x8192) TIFF files each.
The TIFF files for each measurement were converted into a single TTTR like file. Single photon events were created from pixels containing non-zero values. Each photon event was assigned a position along the scanned line (x coordinate) and time after the start of the excitation (t coordinate). The shift between forward and backward lines was optimized by maximizing the correlation between consecutive lines. The resulting data file containing the single photon events based file was then used for our fast multiple-tau direct correlation algorithm, providing the same output as TTTR data.
The obtained spatio-temporal correlation functions (Fig. S3) could be fitted with a single component model and returned expected values for both spot radii (186 nm for confocal and 57 nm for gSTED) and diffusion coefficients (3.85 $\mu m^2 s^{-1}$ and 3.25 $\mu m^2 s^{-1}$). This shows that line-scan FCS data acquisition and analysis can be successfully used with various hardware and data formats. Moreover, line-scan FCS combined with SLBs on glass is a good tool to test the spatial resolution of fluorescence microscopes as single dye molecules are the best approximation of a point source and it is not necessary to correct the obtained resolution values as is the case with fluorescent beads. The main limitation remains the line frequency of the scanner, which must be faster than the average resident time of molecules within the detection spot.

Monte-Carlo simulation of line-scan STED-FCS experiments

To test the performance of the correlation algorithm and to compare the gating and filtering data analysis options for cw STED with gated excitation (gSTED), Monte-Carlo simulations of line scan experiments were performed. Our simulations extend the work of Wohland et al. (10) by adding a resonant line scan and excited state lifetime features. Particles with a fluorescent lifetime of 4 ns and a diffusion coefficient of 2 $\mu m^2 s^{-1}$ were simulated to be subject to 2D Brownian diffusion in a 8 µm x 4 µm rectangle simulation box with periodic boundaries. A fraction of the molecules was allowed to be immobilized and/or to become subject to photobleaching. The simulations were run at 10 MHz clock for 60 s. The Gaussian excitation spot of radius 300 nm was overlaid by a STED donut, which was approximated by a parabolic function, and both are simultaneously scanned along a 4 µm long line with a frequency of 8 kHz. The detection efficiency was assumed to be uniform and the molecular brightness in the centre of the excitation spot with no STED was 100 kHz per molecule. STED represented an additional de-excitation pathway from the excited state of the molecule, the rate of which was position dependent. At each point the decay of the molecule's excited state was assumed to be monoexponential with a rate constant being the sum of the intrinsic fluorescence rate and STED depletion rate. The brightness of the molecule was adjusted accordingly, assuming a fluorescence quantum yield without STED equal to one.

Area integrated correlation function

In molecular diffusion, when the only process taking place is the movement of molecules within the plane, molecules cannot disappear from the image of that plane. This means that the probability of detecting its signal within that plane is constant over time. The spatial-temporal correlation function expresses the probability that a photon from the same molecule at given position and at certain time later is detected. Therefore, for planar diffusion, the sum of correlation values *G(t,x,y)* for all points within the *xy* plane is constant for any correlation time *t*.

$$\iint_{-\infty}^{+\infty} G(t,x,y)dxdy = const \quad (14)$$

The spatial-temporal correlation function for the entire plane (xy) can be obtained through image correlation. As image acquisition is not sufficiently fast, we used line correlation *G(t,r)* where *r* is the distance between the points, which is faster than image correlation and still spatially resolved. If the molecular mobility is isotropic (no direction preferred when averaged over the image and time), a rotational symmetry for the area correlation function can be assumed. Thus the integral of area correlation function can be obtained by integrating the line correlation function along the full angle. This results in:

$$\iint_{-\infty}^{+\infty} G(t,x,y)dxdy = \int_{0}^{+\infty} 2\pi r G(t,r)dr = const \quad (15)$$

The simplest spatio-temporal model of free 2D-diffusion with Gaussian detection areas results in

$$G(t,r) = \frac{A}{4Dt+{w_0}^2} e^{-\frac{r^2}{4Dt+{w_0}^2}} \quad (16)$$

which is a constant value independent of time after integration

$$\int_{0}^{+\infty} 2\pi r \frac{A}{4Dt+{w_0}^2} e^{-\frac{r^2}{4Dt+{w_0}^2}} dx = \left[\pi A e^{-\frac{x^2}{4Dt+{w_0}^2}} + const\right]_{0}^{+\infty} = \pi A. \quad (17)$$

For discrete, uniformly spaced line correlation function of experimental data, the equation to use for calculating the area integrated correlation function $G_A(t)$ for each correlation time t_j is

$$G_A(t_j) = \sum_{i=-n}^{n} x_i G(t_j, x_i) \quad (18)$$

where n is the number of distances for which the temporal correlation is calculated in both directions, resulting in total 2n+1 temporal correlations. The limitation is the finite distance for which the correlations are calculated. This affects mainly the long correlation times at which there is a significant probability that the molecule diffuses out of the maximum correlation distance.

SUPPORTING REFERENCES

1. Ries, J., S. Chiantia, and P. Schwille. 2009. Accurate determination of membrane dynamics with line-scan FCS. Biophys J 96:1999-2008.
2. Digman, M. A., C. M. Brown, A. R. Horwitz, P. Sengupta, W. W. Mantulin, and E. Gratton. 2005. Spatio-temporal fluorescence fluctuation analysis of paxillin-EGFP in cellular adhesions using scanning FCS, ICS and PCH. Biophys J 88:372a-372a.

3. Gregor, I., and J. Enderlein. 2007. Time-resolved methods in biophysics. 3. Fluorescence lifetime correlation spectroscopy. Photoch Photobio Sci 6:13-18.
4. Benda, A., V. Fagul'ová, A. Deyneka, J. Enderlein, and M. Hof. 2006. Fluorescence lifetime correlation spectroscopy combined with lifetime tuning: New perspectives in supported phospholipid bilayer research. Langmuir 22:9580-9585.
5. Böhmer, M., M. Wahl, H. J. Rahn, R. Erdmann, and J. Enderlein. 2002. Time-resolved fluorescence correlation spectroscopy. Chem Phys Lett 353:439-445.
6. Benda, A., P. Kapusta, M. Hof, and K. Gaus. 2014. Fluorescence spectral correlation spectroscopy (FSCS) for probes with highly overlapping emission spectra. Opt Express 22:2973-2988.
7. Felekyan, S., S. Kalinin, A. Valeri, and C. A. M. Seidel. 2009. Filtered FCS and Species Cross Correlation Function. Proc Spie 7183.
8. Štefl, M., A. Benda, I. Gregor, and M. Hof. 2014. The fast polarization modulation based dual-focus fluorescence correlation spectroscopy. Opt Express 22:885-899.
9. Vicidomini, G., A. Schönle, H. Ta, K. Y. Han, G. Moneron, C. Eggeling, and S. W. Hell. 2013. STED nanoscopy with time-gated detection: theoretical and experimental aspects. PloS one 8:e54421.
10. Wohland, T., R. Rigler, and H. Vogel. 2001. The standard deviation in fluorescence correlation spectroscopy. Biophys J 80:2987-2999.
11. Dertinger, T., I. Gregor, I. von der Hocht, R. Erdmann, B. Krämer, F. Koberling, R. Hartmann, and J. Enderlein. 2006. Measuring precise diffusion coefficients with two-focus fluorescence correlation spectroscopy. P Soc Photo-Opt Ins 6092.

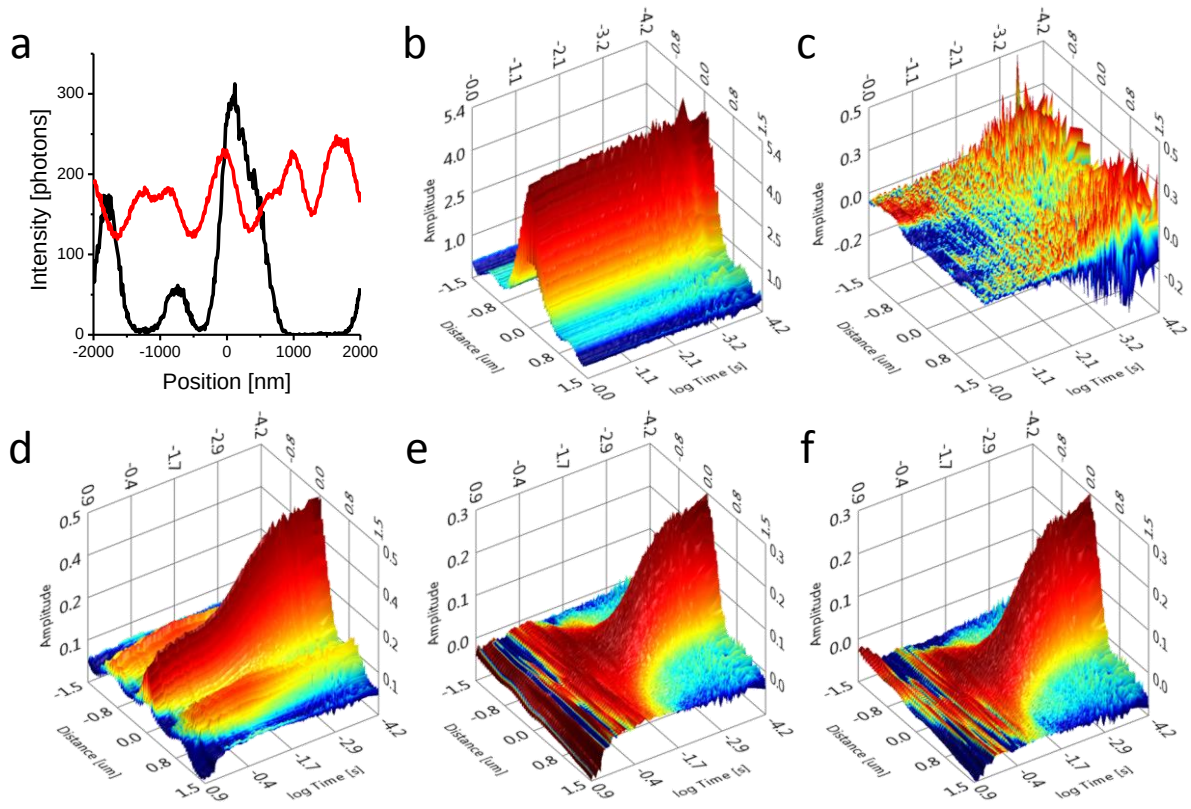

Figure S1 Correction of spatio-temporal correlation functions for heterogeneous immobile fraction and homogenous photobleaching.

(**a**) Intensity profiles along the scanned line for Monte-Carlo simulated data of immobile particles (black line) and a mixture of immobile particles with freely diffusing particles (red line). (**b-c**) The spatio-temporal correlation function of fixed particles without spatial profile correction (b) has a strong time-constant spatial correlation. After the spatial profile correction (c) no spatial correlation is left. (**d-f**) Uncorrected spatio-temporal correlation function (d) for a mixture of freely diffusing particles with slowly photobleached immobile background. The spatial profile correction removes the time constant spatial correlations (e) and subsequent photobleaching correction (f) recovers correlation function for mobile particles only.

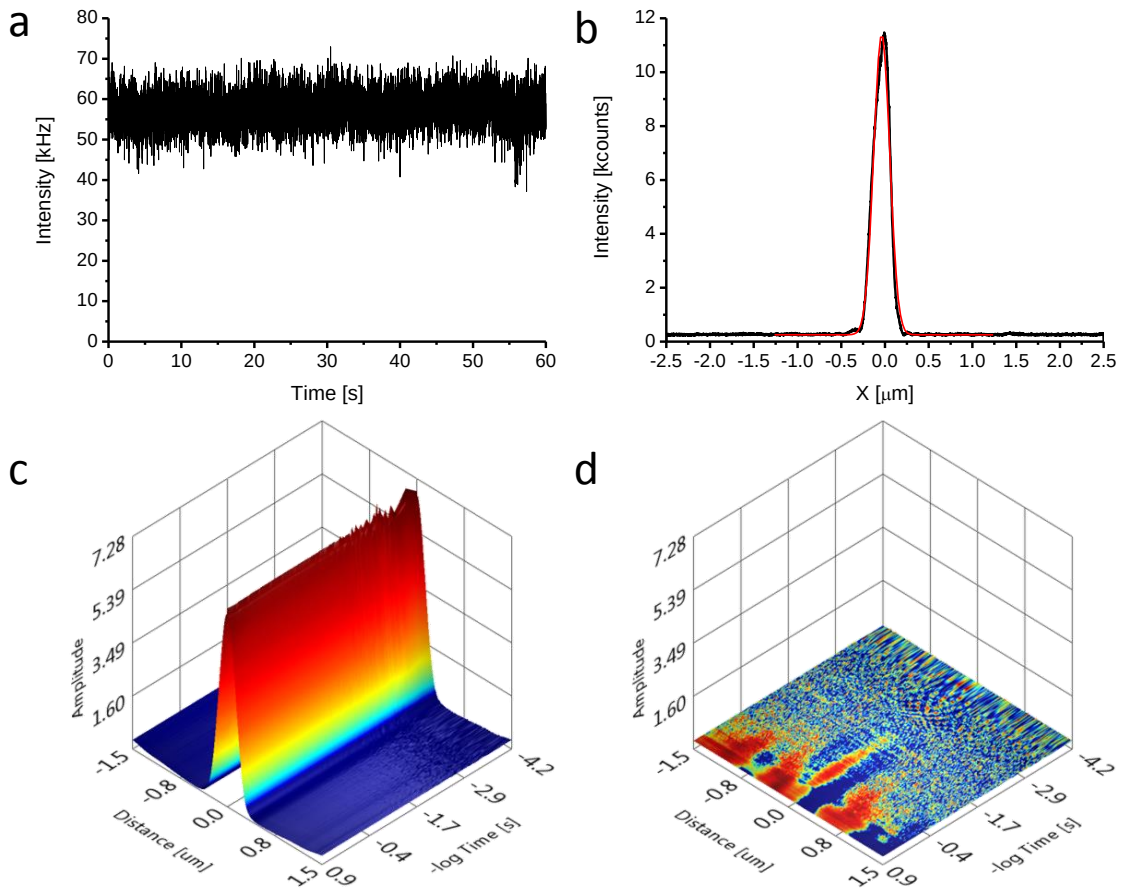

Figure S2 Experimental test of scanner and sample stability.
An immobile gold bead was scanned for 60 s using the standard scan settings (bidirectional resonant line scan, 7920 Hz, 100x oil immersion objective NA1.4, zoom 30x). An excitation light of 640 nm laser was scattered by the bead and after attenuation detected by SPAD detector. (**a-b**) The intensity time trace with 6.3 ms sampling shows no significant trend or oscillations. The spatial profile of the bead along the scanned x-axis (b, black line) is fitted by a Gauss function (b, red line), giving a radius of 185 nm. (**c**) The uncorrected spatio-temporal correlation function has a strong time-constant spatial correlation. (**d**) After the spatial profile correction, no significant correlation can be observed up to 100 ms timescale and only negligible correlations at longer time scales.

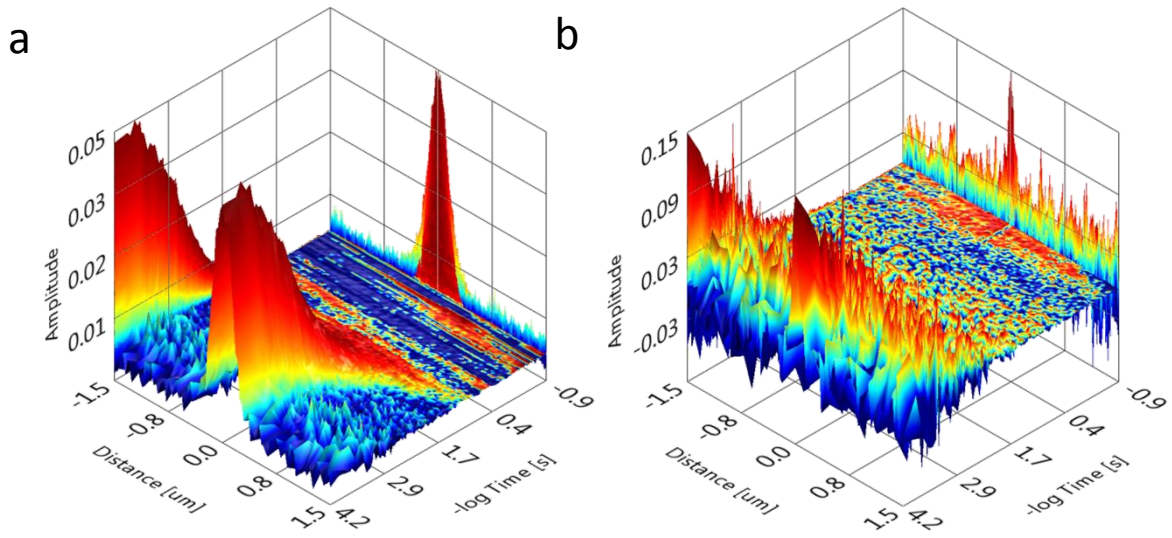

Figure S3 Line-scan gSTED-FCS with TIFF data format.
(**a-b**) Spatio-temporal correlation functions of DOPE-Atto488 in SLBs (DOPC:DOPS 4:1, dye to lipid ratio 1:50 000) on glass measured under confocal (a) and gated-STED conditions (b). The spot radii from the fits are 186 nm and 57 nm for confocal and gated-STED, respectively, and the diffusion coefficients are 3.85 $\mu m^2 s^{-1}$ and 3.25 $\mu m^2 s^{-1}$, respectively.

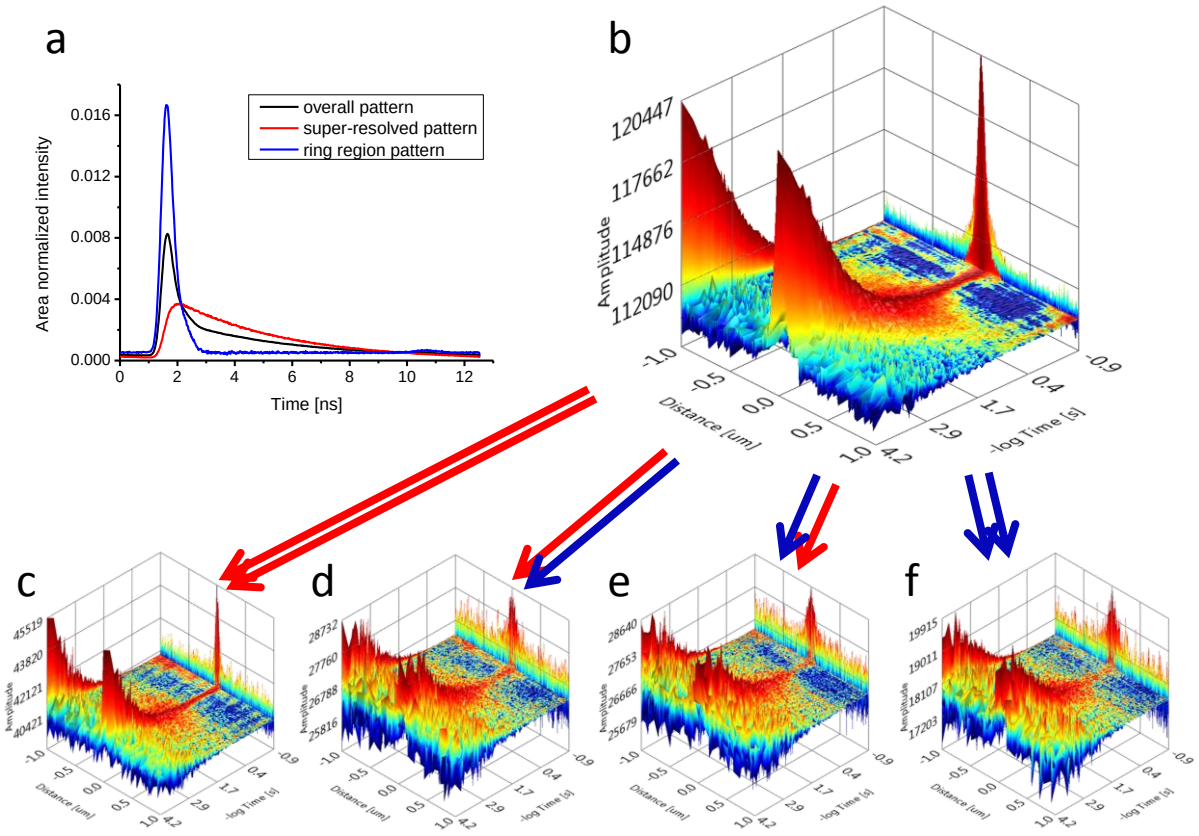

Figure S4 Splitting of the overall spatio-temporal correlation function by filtered FCS. (**a**) The experimentally obtained TCSPC pattern (black line) for DOPE-Atto647N in SLBs made of DOPC on glass (lipid to dye ratio 1:50 000, 640 nm excitation at 10 µW, 750 nm depletion at 100 mW, detection 660-700 m, measurement time 5 min) is a linear combination of TCSPC patterns for fluorescence of non-depleted molecules located in the donut zero region (red line) and a fast decaying component (blue line) originating from fluorescence before depletion in the ring region. (**b**) The overall spatio-temporal correlation function from raw data without filtering. (**c**) The filtered spatio-temporal auto-correlation function for central region fluorescence. (**d**) The filtered spatio-temporal cross-correlation function of the central region and ring fluorescence. (**e**) The filtered spatio-temporal cross-correlation function of the ring and central region fluorescence. (**f**) The filtered spatio-temporal auto-correlation function for ring fluorescence. The presented correlation functions are not intensity normalized. The overall correlation function (b) is a sum of the four filtered correlation functions (c-f). The PSF width for filtered correlation functions is 40 nm (c), 100 nm (d), 95 nm (e) and 130 nm (f).

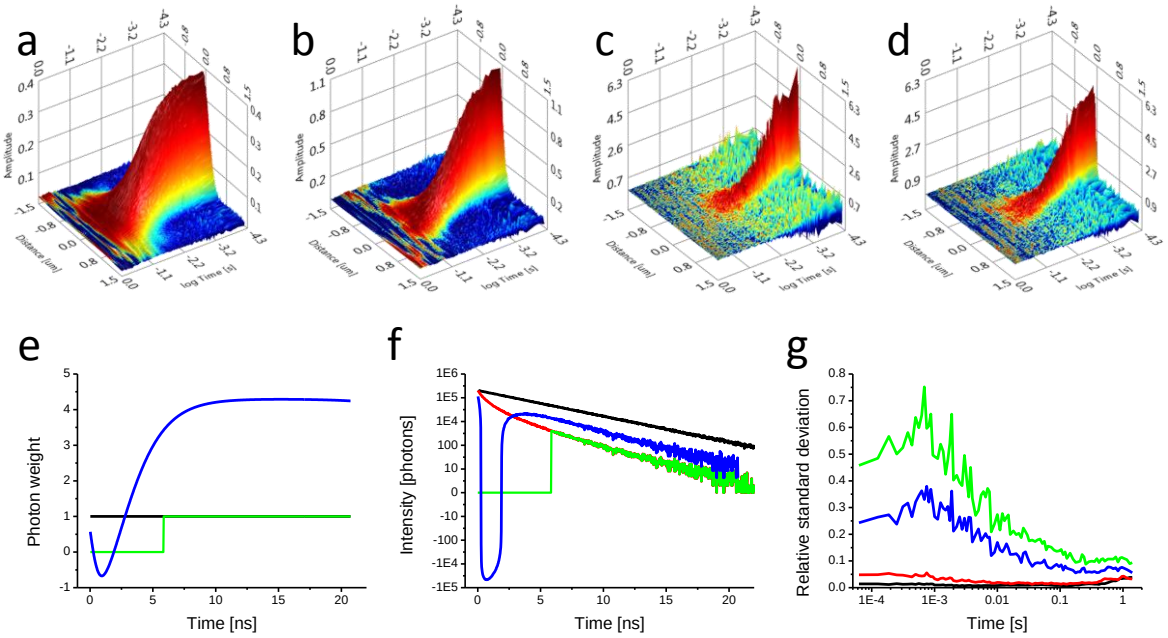

Figure S5 Monte-Carlo simulation of line-scan, filtered cw STED-FCS.
(**a-d**) Spatio-temporal correlation functions for confocal (a), cw STED (b), gated cw STED (c) and filtered cw STED (d) show decreasing PSF width from 300 nm for confocal, 175 nm for cw STED down to 75 nm for gated and filtered cw STED. The fitted diffusion coefficient is 2 $\mu m^2 s^{-1}$ for all cases. (**e**) Filters for photon weighting based on the photon arrival time after excitation. Confocal and cw STED uses all photons equally (black line), gated cw discards photons arriving before 6 ns (green line) and filtered cw STED weights photon by a filter calculated for the longest decay component (blue line). (**f**) TCSPC histograms show that the confocal signal is mono-exponential (black line) whereas the cw STED signal is multi-exponential (red line) due to the cw depletion. The gated cw STED histogram contains only the late arriving photons (green line) and filtered cw STED histogram (blue line) enhances late photons but uses the whole data range. (**g**) Both gating and filtering can achieve identical resolution (75 nm in this case, no background included in simulations), but filtering (blue line) is more efficient in relation to signal usage and the obtained correlations have almost two times lower relative standard deviation than gating (green line).

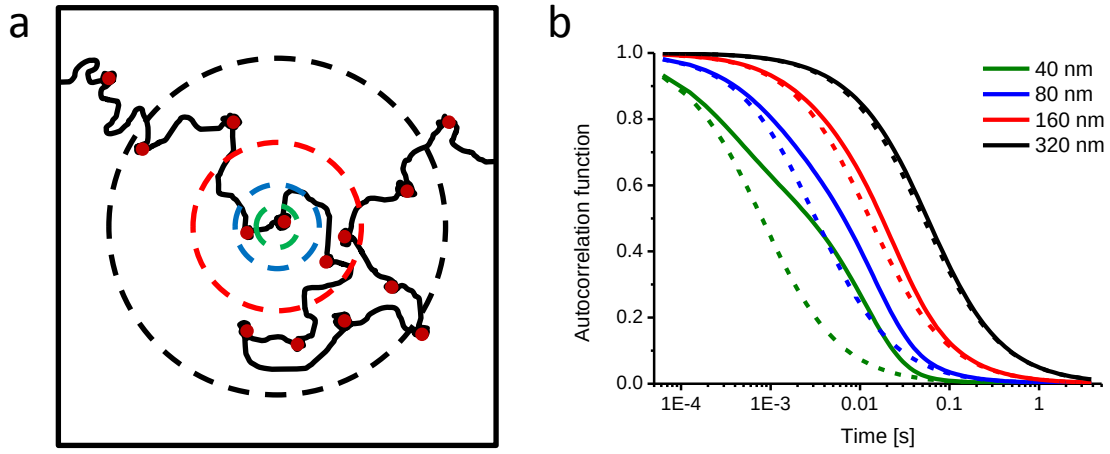

Figure S6 Principle of variable spot STED-FCS with transient binding.
(**a**) Schematic of particle diffusion with transient trapping (red dots) in detection spots of variable radius (dotted circles: 320 nm radius black, 160 nm radius red, 80 nm radius blue and 40 nm radius green). (**b**) Autocorrelation functions for laterally diffusing molecules (D = 1 $\mu m^2 s^{-1}$) that are transiently trapped at random locations (k_{on} = 100 s^{-1}, k_{off} = 100 s^{-1}) for varying detection spot radius (solid lines: 320 nm radius black, 160 nm radius red, 80 nm radius blue and 40 nm radius green). The calculation is based on the diffusion model described in Dertinger et al. (11). Autocorrelation functions for two times slower free diffusion (D = 0.5 $\mu m^2 s^{-1}$, dash lines) are shown for comparison. The time resolution of the calculations is identical to the time resolution of line scan FCS, spot size are matched to experimentally obtainable spot sizes and the diffusion coefficient is set to a typical value observed for labelled lipids in the plasma membrane.

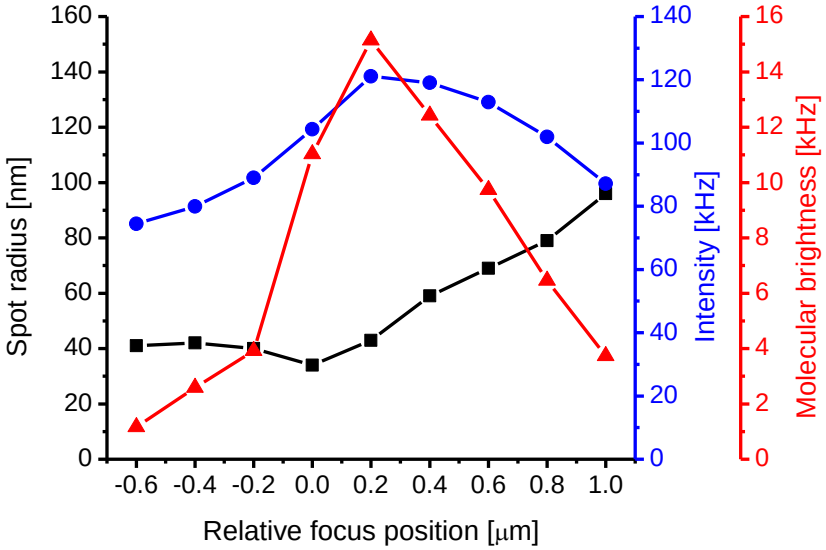

Figure S7 Axial dependence of STED-FCS measurements.
SLBs made of DOPC on glass and labelled with DOPE-Atto647N in lipid to dye ratio 1:100 000 were measured by line-scan STED-FCS (640 nm excitation at 10 µW, 750 nm depletion at 100 mW, detection 660-700 m, filtered correlation) at different focus positions (axial direction) relative to the sample. Axial dependence of spot radius (black squares), overall fluorescence intensity (blue circles) and the apparent molecular brightness (red triangles) on the focus position relative to the sample position are shown. Data indicate that the position of the best spatial resolution does not have to coincide with the position of the highest detected overall intensity. A small misalignment along the z-axis (400 nm) can cause a significant difference in actual spot radius (from 40 nm to 60 nm).

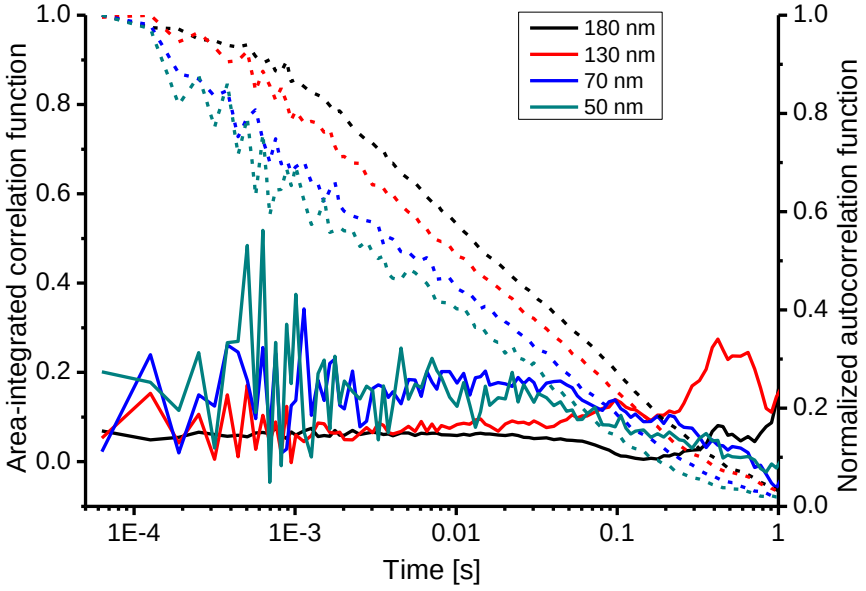

Figure S8 Area-integrated correlation function.
Area-integrated correlation functions (solid lines) and temporal autocorrelation functions (dashed lines) for DOPE-Atto647N in supported lipid bilayers on glass (DOPC:DOPS 4:1, lipid to dye ratio 20 000:1, 640 nm excitation at 10 µW) at increasing STED powers, decreasing the spot radius from 180 nm (black line) to 130 nm (red line), 70 nm (blue line) and 50 nm (dark green line). The constant values of area-integrated correlation functions at short times for each spot size are indicative that the fast decays of the temporal autocorrelation functions are not related to dye photo-physics induced by the intensive STED laser but indeed caused by 2D diffusion.

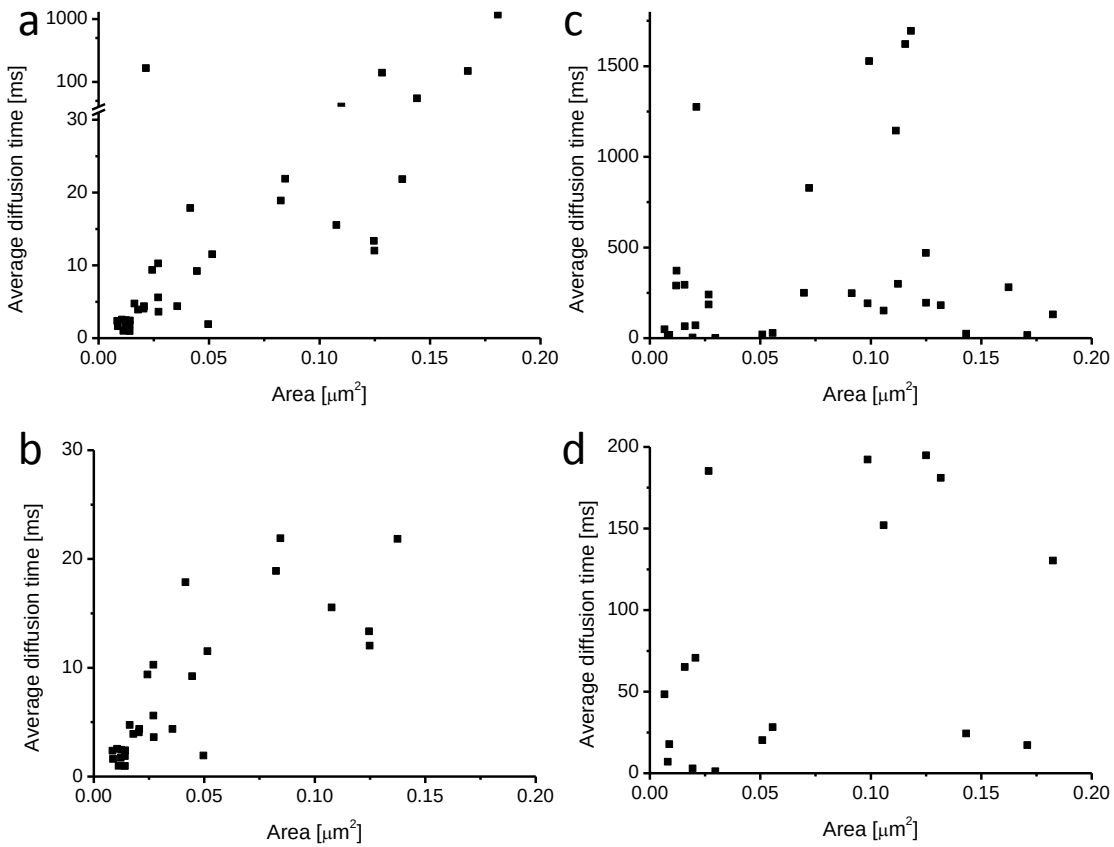

Figure S9 Variable spot STED-FCS in cells.
The average diffusion time is plotted against the spot area for DOPE-Atto647N (**a-b**) and Atto647N-SM (**c-d**) in COS7 cells. Each data point represents one measurement. The lower graphs (b, d) are zooms of graphs (a, c). The raw data are identical to the raw data used in Figure 5a and 5b. The average diffusion time was obtained as the time at which the correlation function at zero spatial difference declines to a half of its value at zero lag time. The spot area was obtained from the spot radius at zero lag time using a Gaussian approximation.

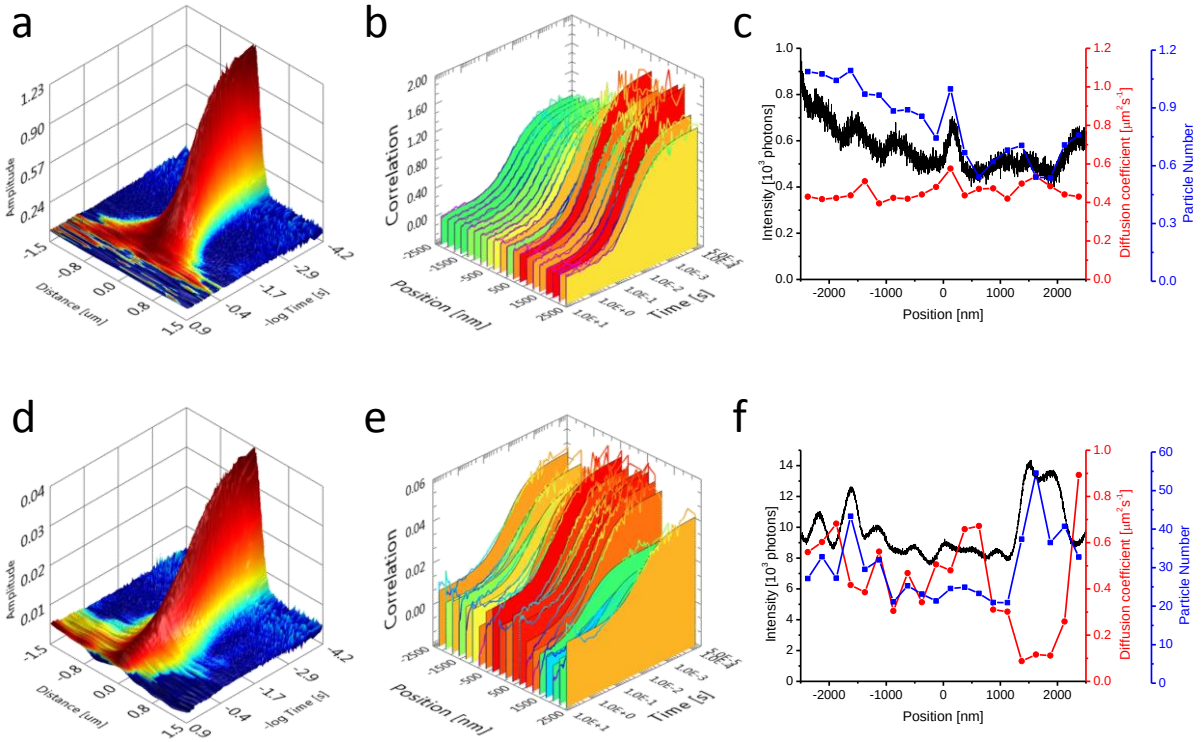

Figure S10 Comparison of DOPE-Atto647N with DOPE-Oregon Green 488.
Confocal line scan FCS was performed on the plasma membrane of HeLa cells. The cells were labelled either with DOPE-Oregon Green 488 (**a-c**) or with DOPE-Atto647N (**d-f**). For DOPE-Oregon Green 488 acquisitions, the 488 nm line of cw Argon laser at 5 µW, emission bandpass filter HQ525/50 and 7.92 kHz bidirectional resonant scanner were used. For DOPE-Atto647N acquisitions, a 640 nm pulsed laser at 5 µW, emission bandpass filter HQ680/40 and 7.92 kHz bidirectional resonant scanner were used. The spatio-temporal correlation function for DOPE-Oregon Green 488 (**a**) could be fitted to a one-component model (D = 0.44 $\mu m^2 s^{-1}$, w_0 = 172 nm), the spatio-temporal correlation function for DOPE-Atto647N (**d**) needed a two-component model (D_{fast} = 0.727 $\mu m^2 s^{-1}$, D_{slow} = 0.013 $\mu m^2 s^{-1}$, w_0 = 197 nm). Temporal autocorrelation functions (**b, e**) at different points along the scanned line were fit using a single component model. (**c, f**) The diffusion coefficients and particle numbers (obtained from the one-component fit, b and e) are plotted together with the overall fluorescence intensity as a function of the position along the line. The average diffusion coefficient for DOPE-Oregon Green 488 was 0.457 ± 0.05 $\mu m^2 s^{-1}$; the average diffusion coefficient for DOPE-Atto647N was 0.436 ± 0.21 $\mu m^2 s^{-1}$.